Nanoscale organization of luminescent materials and their polarization properties investigated by two-dimensional polarization imaging

Shi, Juanzi

2021

Document Version:
Publisher's PDF, also known as Version of record

Nanoscale organization of luminescent materials and their polarization properties investigated by two-dimensional polarization imaging

JUANZI SHI
CHEMICAL PHYSICS | FACULTY OF SCIENCE | LUND UNIVERSITY

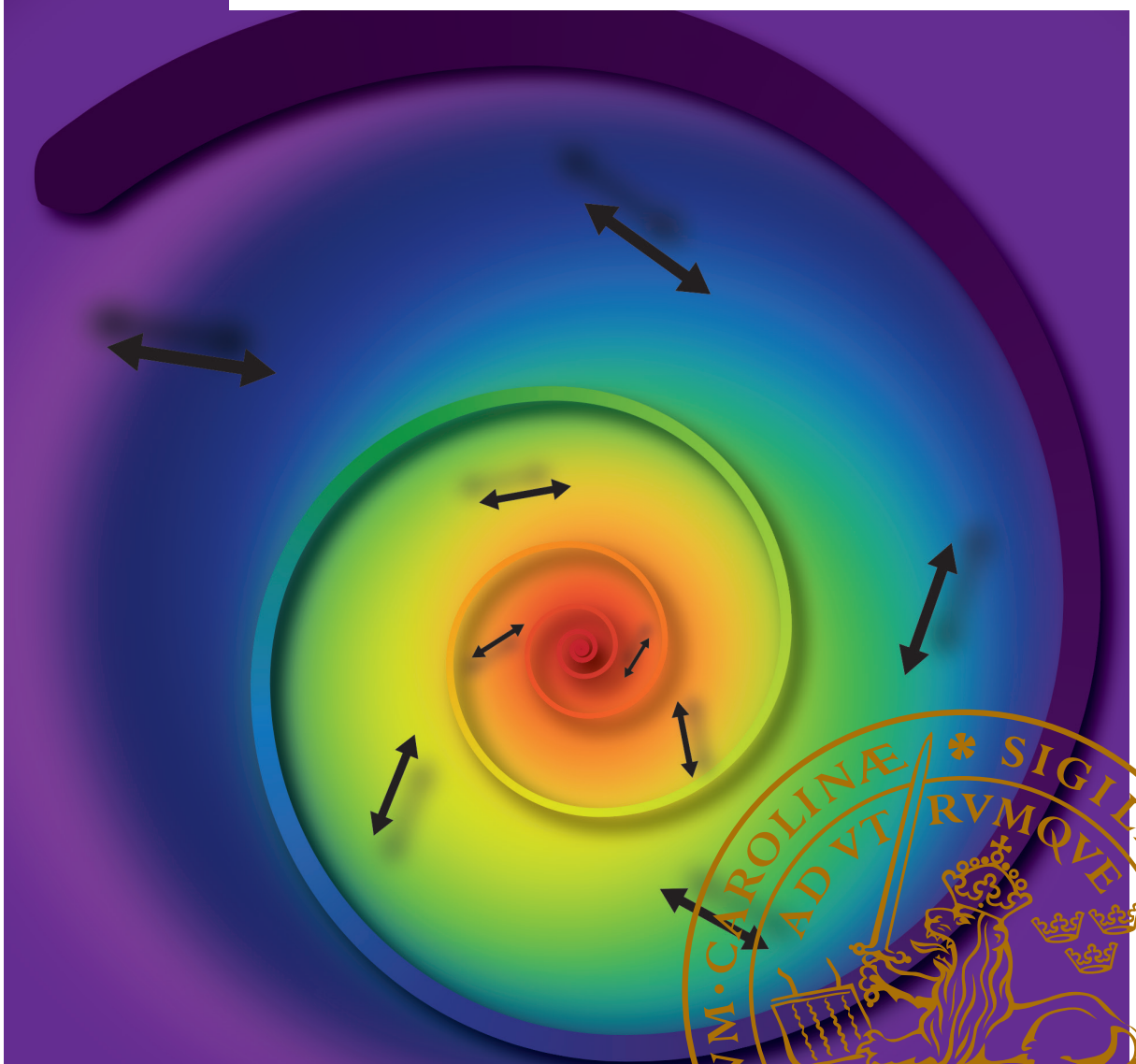

Printed by Media-Tryck, Lund 2021 NORDIC SWAN ECOLABEL 3041 0903

Faculty of Science
Department of Chemistry
Division of Chemical Physics

ISBN 978-91-7422-818-2

Nanoscale organization of luminescent materials and their polarization properties investigated by two-dimensional polarization imaging

Juanzi Shi

LUND UNIVERSITY

DOCTORAL DISSERTATION

by due permission of the Faculty of Science, Lund University, Sweden.
To be defended at Lecture hall C, Kemicentrum, Naturvetarvägen 16, 22362 Lund,
Friday 18th of June of 2021 at 9.15 am.

Faculty opponent
Researcher Mariano Campoy-Quiles

Organization
LUND UNIVERSITY
Division of Chemical Physics
Department of Chemistry
P. O. BOX 124, SE-22100 Lund, Sweden

Document name
Doctoral Dissertation

Date of issue
18th June 2021

Author(s)
Juanzi Shi

Sponsoring organization

Title and subtitle
Nanoscale organization of luminescent materials and their polarization properties investigated by two-dimensional polarization imaging

Abstract
Semiconductor materials (e.g., conjugated polymers, metal halide perovskites) have been widely used in solar cells, light-emitting diodes, and photodetectors. Organic conjugated systems have high mechanical flexibility and low costs for production. Metal halide perovskites have the advantage of strong light absorption, long charge-carrier diffusion lengths, and low intrinsic surface recombination.

Polarization-sensitive single-molecule methods have been extensively used to study the chromophore organization and excitation energy transfer (EET) process. Our novel polarization technique, two-dimensional polarization imaging (2D POLIM) is designed to simultaneously measure and control both the excitation and emission polarization characteristics of an individual object. A model based on single funnel approximation (SFA) is applied to fit the 2D polarization portrait obtained from 2D POLIM measurements. 2D POLIM in combination with the SFA model allows the quantitative characterization of EET efficiency. Overall, A large number of polarization parameters, e.g., modulation depths, phases, luminescence shift, fluorescence anisotropy, energy funneling efficiency, and properties of the EET-emitter, can be extracted from 2D polarization portraits. They give a full picture of chromophores' organization and a quantitative measure of the EET process.

In this thesis, we applied the 2D POLIM technique to investigate the fundamental optoelectronic process in different types of luminescent materials. H-aggregates forming in spin-cast conjugated films are visualized by modulation depth and phase imaging contrast. Light-harvesting efficiency shows the efficient ET within the amorphous phase and poor ET between H-aggregates due to the less overlap between absorption and emission spectra. Together with single-molecule spectroscopy and scanning electron microscope, we studied the polarization property of individual $MAPbBr_3$ aggregates, which shows the well-known dielectric screening effect cannot fully explain the absorption polarization from weakly elongated objects (even with irregular shapes). We propose that power-dependent quantum yield can further increase the modulation depth of excitation. 2D POLIM was also applied to explore the aggregation state of proteins in the biological system. Furthermore, we did a series of computer experiments to examine and improve the SFA model. We break the limit of energy funneling efficiency and propose an asymmetric three-dipole model, which is more applicable for multi-chromophore systems. In the future, quantitative phase-contrast imaging and time-resolved 2D POLIM might be further developed.

Key words
Polarization, energy transfer, single-molecule microscopy, π-conjugated polymer, perovskite

Classification system and/or index terms (if any)

Supplementary bibliographical information

Language
English

ISSN and key title

ISBN
Printed version: 978-91-7422-818-2
Digital version: 978-91-7422-819-9

Recipient's notes

Number of pages 211

Price

Security classification

Signature: Juanzi Shi

Date: 7th May 2021

Nanoscale organization of luminescent materials and their polarization properties investigated by two-dimensional polarization imaging

Juanzi Shi

LUND
UNIVERSITY

Coverphoto by Weihua Lin and Juanzi Shi

Division of Chemical Physics
Department of Chemistry
Faculty of Science

ISBN 978-91-7422-818-2
ISSN 978-91-7422-819-9

Printed in Sweden by Media-Tryck, Lund University
Lund 2021

‘I like to think that maybe one day you’ll be an old man like me, talking a younger man’s ear off, explaining to him how you took the sourest lemon that life has to offer and turned it into something resembling lemonade.’

-- From ‘This is us’

Table of Contents

Abstract

Semiconductor materials (e.g., conjugated polymers, metal halide perovskites) have been widely used in solar cells, light-emitting diodes, and photodetectors. Organic conjugated systems have high mechanical flexibility and low costs for production. Metal halide perovskites have the advantage of strong light absorption, long charge-carrier diffusion lengths, and low intrinsic surface recombination.

Polarization-sensitive single-molecule methods have been extensively used to study the chromophore organization and excitation energy transfer (EET) process. Our novel polarization technique, two-dimensional polarization imaging (2D POLIM) is designed to simultaneously measure and control both the excitation and emission polarization characteristics of an individual object. A model based on single funnel approximation (SFA) is applied to fit the 2D polarization portrait obtained from 2D POLIM measurements. 2D POLIM in combination with the SFA model allows the quantitative characterization of EET efficiency. Overall, A large number of polarization parameters, e.g., modulation depths, phases, luminescence shift, fluorescence anisotropy, energy funneling efficiency, and properties of the EET-emitter, can be extracted from 2D polarization portraits. They give a full picture of chromophores' organization and a quantitative measure of the EET process.

In this thesis, we applied the 2D POLIM technique to investigate the fundamental optoelectronic process in different types of luminescent materials. H-aggregates forming in spin-cast conjugated films are visualized by modulation depth and phase imaging contrast. Light-harvesting efficiency shows the efficient ET within the amorphous phase and poor ET between H-aggregates due to the less overlap between absorption and emission spectra. Together with single-molecule spectroscopy and scanning electron microscope, we studied the polarization property of individual $MAPbBr_3$ aggregates, which shows the well-known dielectric screening effect cannot fully explain the absorption polarization from weakly elongated objects (even with irregular shapes). We propose that power-dependent quantum yield can further increase the modulation depth of excitation. 2D POLIM was also applied to explore the aggregation state of proteins in the biological system. Furthermore, we did a series of computer experiments to examine and improve the SFA model. We break the limit of energy funneling efficiency and propose an asymmetric three-dipole model, which is more applicable for multi-chromophore systems. In the future, quantitative phase-contrast imaging and time-resolved 2D POLIM might be further developed.

Popular Science Summary

Green plants can capture solar energy and use solar energy to convert water, carbon dioxide, and minerals into energy-rich organic compounds. Imitating green plants, people invented solar cells to capture sunlight and convert the light energy directly into electricity. Solar cells are generally made of semiconductor materials. The semiconductor materials studied in this thesis are conjugated polymers and metal halide perovskites. The understanding of these materials can help us to create more efficient solar-based devices. We are particularly interested in the internal organization and energy exchange within luminescent materials.

We use the single-molecule microscopy technique, which allows us to study individual objects (e.g., molecules, nanocrystals). Single-molecule imaging reveals more details about the behavior of individual objects that would be hidden by a large group of molecules. For example, there are piles of snow in the north of Sweden during the winter. By taking a normal picture, you see a white world. However, if we take a close look with a microscope, we can see snowflakes in a dazzling variety of shapes. It is always exciting to notice the difference between individuals.

To characterize the orientation of objects and the excitation energy transfer between them, we use light polarization. The polarization of light is the orientation of the electric field vector. The projection of the electric field vector of a linearly polarized light on a plane has only one orientation. We can use some filters with a specific transmission axis to select the light. For example, polarized sunglasses that use to selective block sunlight reflected from surfaces. Or we can think the filter is like the small elongated gap of a piggy bank. A coin (orientation of electric field vector) can only pass through if it is parallel to the small gap's elongation (transmission axis).

Base on the above idea, we can learn the orientation of objects from their absorption polarization. If the objects are aligned on one orientation, they will have a preferential absorption along with one specific orientation. However, if the objects are randomly oriented, then they will absorb all polarization orientations equally.

Furthermore, we can use the difference between absorption and fluorescence emission to study the energy transfer process within an object. It is like one puts an orange (input-incident light) into a juicer machine (studied system), and then juice (output-fluorescence emission) comes out. Since there is an obvious difference

between input and output, we can guess something (e.g., energy transfer) must happen in the system.

Now consider molecules are excited by linearly polarized light at an angle φ. The molecules that are oriented along this direction are preferentially excited. Without energy transfer, the fluorescence emission should also be polarized at angle φ. However, if molecules exchange energy efficiently, or all the energy transfers to one molecule and emits there. Then the emission would become partially polarized or polarized at another angle. By further quantitatively study the difference between input and output, we can calculate the energy transfer efficiency.

Combing single-molecule microscopy and light polarization, we develop a technique called two-dimensional polarization imaging. This technique allows us to obtain the orientation and the information of the energy transfer process of an individual object. Furthermore, based on a mathematical model (single funnel approximation), we can quantitatively estimate the energy transfer efficiency in the system.

Acknowledgments

This is an impressive and exciting part of my thesis for myself. After writing it, I realized how lucky and how happy I am during the last four years.

First, I would like to start by thanking my supervisor Ivan Scheblykin. I respect and appreciate your responsibility, honesty, critical thinking, and kindness. You taught me the reality is neither 'white' nor 'black', but 'grey'. You also taught me how to split and simplify a complicated problem and how to judge the accuracy of one measurement through some simple tests. All of them are precious experiences for my future life and career. Moreover, thank you for giving me the chance to come to Sweden. This is a completely fresh and exciting beginning. Also, I give my thanks to my unofficial 'second' supervisor Ruiyun. Thanks for guiding me and asking me 'why do you make this change?' Thanks for teaching and explaining to me the principle of TCSPC in such detail. I miss our trips, sports, and cooking. I feel so lucky to meet you in Lund.

Thanks to all the (single-molecule spectroscopy) SMS group members. You build up the largest part of my life and make me feel at home. Daniela, my good friend, thanks for your kindness and passion for helping me start my new life here. It was too joyful to play squash, ice skating, and running together. And my good friend Marina, thanks for the company and delicious food every Sunday night. I will never forget that we had so impressive and beautiful trips, to your hometown (Christmas) and my hometown (The Great Wall). Hope you still drink warm water sometimes. And Bruce, comrade-in-arms, thanks for the 4.5 years company. I sincerely wish you a bright future. Sudipta, thanks for bringing so much fun into the office, all the inspired and interesting discussions, and 'irritations'. And Chen, I always enjoy scientific discussions with you. They are as 'delicious' as the baked pork you made! Moreover, thanks to our previous group member Rafael, you have done such excellent Ph.D. work. I learned too much from it, especially the program you wrote. Thanks to all the SMS group members, Aboma, Boris, Alexander, Aymen, Shraddha, Klara, Safi, you are coworkers and friends. Hope we have more SMS parties to cheers for science, music, and sports (SMS)!

To all my friends: Qi Shi, Haoran Yu, Xin Liu, Haiyue Gong, Maria, Chuanshuai Li, Xiaoyan Xu (and Zhuangzhuang), Xianshao Zou, Fan Wu, Jingyuan Zhu, Yong Li, Yao Wang, Yuchen Liu, Zehan Yao, Yue Wu, Yuhan Ma, Meiyuan Guo, Yunqian Zhong. Thank you all for bringing me happiness and making my life as

beautiful as the northern lights. And to my 'little Mameshiba', you are the piece that surprisingly completes my puzzle.

Furthermore, I also would like to thank our collaborators: Olle Inganäs, Pavel Frantsuzov, Yuxi Tian, Ellen Moons, Haizheng Zhong, Maria Messing, Igor Zabronsky, Xiaofeng, Xu, Xiangang Wu, Yuxin Xia, Wengao Lu, Zafer Hawash, Dargie Deribew, I would not be able to do the science without your supports, contributions, and help.

I am also grateful to all the people that shared this time with me in the chemical physics division. It was so much fun to have science day, Fika, celebrate Christmas, hotpot party, and dumpling party with all of you. Thanks for those beautiful and joyful memories.

致我的父母和家人: 你们安好，便是晴天。

List of publications

This thesis is based on the following papers, which will be referred to in the text by Roman numerals.

I. Photo-Oxidation reveals H-aggregates hidden in spin-cast conjugated polymer films as observed by two-dimensional polarization imaging.
Shi, J., Xu, X., Xia, Y., Chen, R., Hawash, Z., Deribew, D., Moons, E., Inganäs, O. & Scheblykin, I. G.
Chemistry of Materials, *31*(21), 8927–8936 (2019).

II. Photoluminescence polarization of $MAPbBr_3$ nanostructures. Does dielectric screening effect explain it?
Shi, J., Ryabov, I., Seth, S., Frantsuzov, P., Zinedine, S., Andreas, W., Messing, M., Wu, X., Lu, W., Zhong, H. & Scheblykin, I. G.
Manuscript. (2021).

III. Quantitative assessment of energy transfer efficiency by two-dimensional polarization imaging using single funnel approximation.
Shi, J., Camacho, R. & Scheblykin, I. G.
Manuscript. (2021).

IV. 2D polarization imaging as a low-cost fluorescence in models of Parkinson's disease method to detect α-synuclein aggregation ex vivo in models of Parkinson's disease.
Camacho, R., Täuber, D., Hansen, C., **Shi, J.**, Bousset, L., Melki, R., Li, J., Scheblykin, I. G.
Communications Biology, *1*, 157. (2018).

My Contribution to the Publications

I. I adapted the fluorescence microscope for the polarization, fluorescence spectra and lifetime measurements. I analyzed the data and did the calculation of the two-phase model. I prepared all the figures and took part in the writing of the paper.

II. Together with co-authors, I prepared the composite films. I did the two-dimensional polarization imaging (2D POLIM) and SEM measurements. I did the data analysis and found the correlation between PL and SEM images. I joined actively in the discussion of the simulation section. I prepared all the figures and took part in the writing of the paper.

III. I wrote the program in python to check and further improve the SFA model which was established previously by R. Camacho et al. I prepared the figures and wrote the article.

IV. I performed and analyzed complementary experiments on conjugated polymer films to demonstrate the advantage of single funneling efficiency in comparison with traditional parameter fluorescence anisotropy.

Abbreviations

LCD – Liquid Crystal Display

NP – Nanoparticle

LD – Linear Dichroism

FDLD – Fluorescence Detected Linear Dichroism

LCAO – Linear Combination of Atomic Orbitals

TDM – Transition Dipole Moment

VB – Valence Band

CB – Conduction Band

FRET – Förster Resonance Energy Transfer

ET – Energy Transfer

EM-CCD – Electron Multiplying Charge-Coupled Device

TCSPC – Time-Correlated Single-Photon Counting

APD – Avalanche Photodiode

2D POLIM – Two-Dimensional Polarization Imaging

M_{ex} – Fluorescence Excitation Modulation Depth

M_{em} – Fluorescence Emission Modulation Depth

θ_{ex} – Fluorescence Excitation Phase

θ_{em} – Fluorescence Emission Phase

LS – Luminescence Shift

ε – Energy Funneling Efficiency

r – Fluorescence Anisotropy

CP – Conjugated Polymer

AFM – Atomic Force Microscopy

Chapter 1 Introduction

1.1 Light polarization

The effect of light polarization is widely used in science and technology and can be noticed even in our daily life (**Figure 1.1**). Implementing polarization control can be used to eliminate glare from light reflection (**Figure 1.1a**). Light reflected from horizontal surfaces, such as snow, road, leaves, or water, is partially horizontally polarized according to Fresnel equations. Thus, a polarizer oriented vertically can block a substantial part of the reflected light from such surfaces. This effect is used in polarized sunglasses to reduce glare and protect our eyes. Furthermore, a polarizer placed in front of a camera can reduce shiny reflections and bring more intense color or contrast to the image. Polarization is also used in the entertainment industry to produce 3D movies (**Figure 1.1b**). Two movies are filmed from two slightly different camera locations. Each movie is projected through a polarizing filter with orientations perpendicular to each other. The audiences wear special glasses with vertically (for one eye) and horizontally (for the other eye) oriented polarization filters. Consequently, one eye sees the movie projected from one projector while the other eye sees it from the other projector, which gives the viewer a perception of 3D depth. Another important application of polarization is a liquid crystal display (LCD), where a liquid crystal material is sandwiched between two crossed polarizers. Without applying voltage, the liquid crystal molecules are aligned perpendicular to the surface of the polarizers. The second polarizer blocks the linearly polarized light coming through the first polarizer. When a voltage is applied, the orientation of crystal molecules is changed (**Figure 1.1c**), resulting in light polarization rotation after passing the liquid crystal. Thus, a certain amount of light will pass through the second polarizer depending on the applied voltage. This is how one pixel of an LCD screen is constructed. In industry, polarization control is widely used to perform stress analysis tests on transparent plastics (**Figure 1.1d**) because most of them become birefringent when put under stress. By building a model and then putting it under stress, the pattern visible between crossed polarizers can show large stress areas with the highest risk of material breakdown. The change of refractive index depends on the wavelength of the light. That is why the pattern is colored. So, all we see is a map of the stress in the sample.

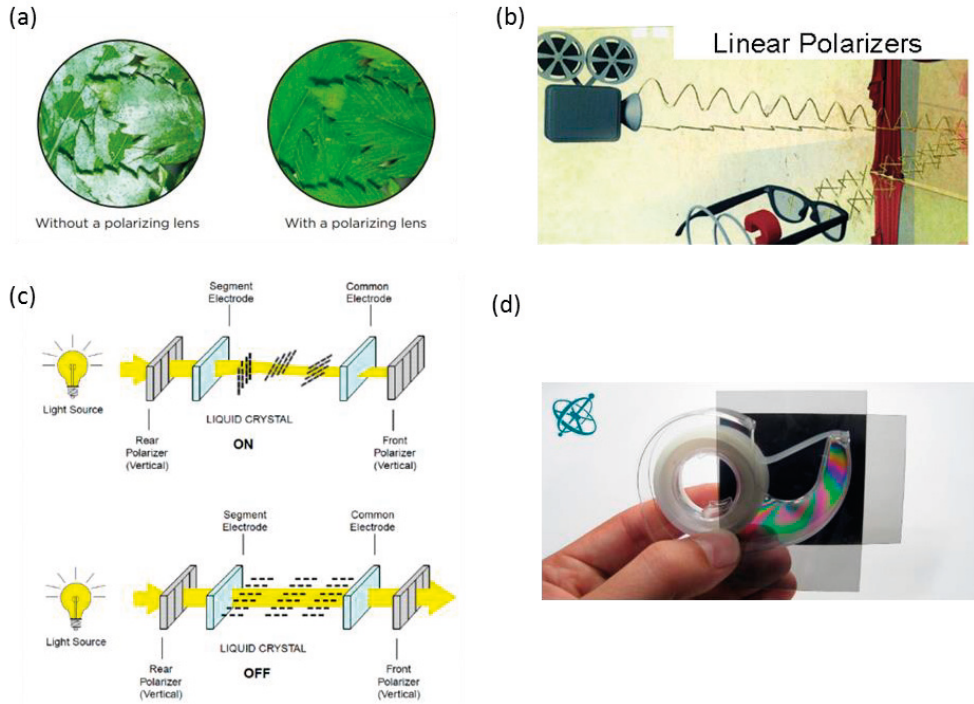

Figure 1.1. The application of light polarization for (a) glare reduction (b) 3D movie, (c) liquid crystal display (LCD), and (d) stress analysis of transparent materials
(source: https://www.scienceworld.ca/resource/polarizing-filters)
(source: https://www.pcmag.com/encyclopedia/term/polarized-3d)
(source: https://electrosome.com/lcd-display-fundamentals/)
(source:https://www.sciensation.org/hands-on_experiments)

Light polarization plays an important role in modern diverse optics application which is widely used in fundamental scientific research, such as ultrafast optical switching,[1] polarization-sensitive photodetection,[2] optical antennas,[3] polarized light-emitting diodes[4] and so on. It is worth noticing that light polarization and anisotropic absorption/emission have been applied in the field of optical super-resolution microscopy. The method is called super-resolution by polarization demodulation/excitation polarization angle narrowing (SPoD-ExPAN). The resolution of SPoD-ExPAN is about 2-3 times better than the diffraction limit, and it can be applied for large biological structures without the need for blinking. The main idea of this method is that differently oriented fluorescent dyes emit periodic signals peaking at different times by being excited with rotating linearly polarized light.[5] Furthermore, birefringence and dichroism reveal anisotropic crystal structure.[6] Linear dichroism and fluorescence anisotropy indicate fundamental

electronic processes in photoactive materials.[7] Overall, light polarization is widely used in scientific research.

1.1.1 The nature of light polarization

The nature of light has been a debate for centuries. Nowadays, the view of the wave-particle duality of photons is most commonly held. Wave-particle duality describes that light travels as photons, and these photons can act like waves (e.g., interference) or particles (e.g., photoelectric effect). This concept has been proved by an elegant experiment carried by Philippe Grangier et al. in 1986.[8] A low-intensity light source and two detectors were set to generate and detect single photons. The light passes through a beam splitter that reflects 50% of the photons onto a path-oriented 90 degree to the original path. The remaining 50% of the photons were transmitted through the beam splitter. As a result, each detector has a 50% probability of recording an event but no chance of both responding. However, if the light was recombined before they arrive at detectors by means of Mach-Zehnder interferometer, one of the detectors can always record an event. Whereas another one can never record an event because of the constructive and destructive interference of waves. From this experiment, wavelike property and particle-like property seem to be complementary aspects of light.

Light is electromagnetic radiation, an electric field that oscillates in both time and space, and a corresponding orthogonal magnetic field oscillates with the same spatial and temporal periodicity. In the following study, we just consider the electric field (**Figure 1.2**). A linearly polarized light propagating along the z-axis and oscillating along the x-axis can be represented by:[6]

$$E_x(z,t) = E_x^0 \, cos \, cos \, (kz - \omega t)\hat{\imath} \tag{1.1}$$

E_x^0 is the amplitude of the electric field, $k = 2\pi/\lambda$ is wave number, $\omega = 2\pi\nu$ is circular frequency, and $\hat{\imath}$ is the unit vector along x axis. Similarly, linearly polarized light with electric field oscillating along y-axis is given by:

$$E_y(z,t) = E_y^0 \, cos \, cos \, (kz - \omega t + \phi)\hat{\jmath} \tag{1.2}$$

Here $\hat{\jmath}$ is a unit vector along the y axis, and φ is the relative phase different between the two waves. The sum of these two perpendicular waves is:

$$E(z,t) = E_x(z,t) + E_y(z,t) \tag{1.3}$$

By varying the relative phase φ and amplitude E_x^0, linearly polarized light ($\varphi = 0$), circularly polarized light ($\varphi = \pm\pi/2$, $E_x^0 = E_y^0$), and elliptically polarized light ($\varphi \neq 0$ and $\varphi \neq \pm\pi/2$) can be generated.

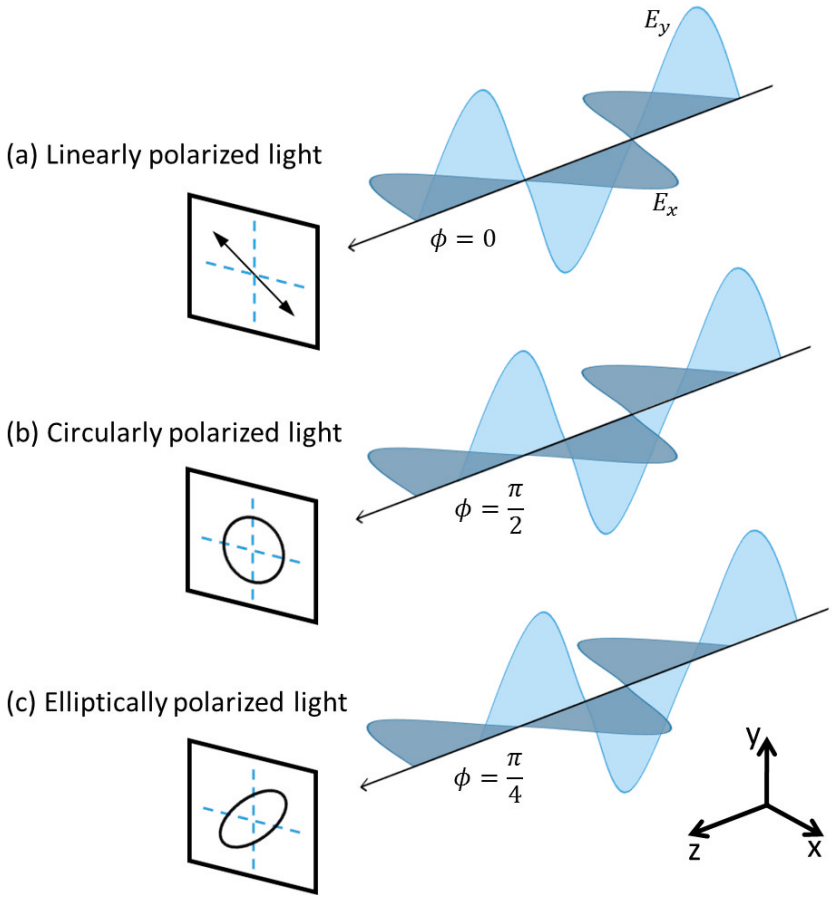

Figure 1.2. (a) linearly polarized light, φ = 0 (b) circularly polarized light, φ = π/2 (c) elliptically polarized light φ = π/4.

1.1.2 Simple manipulation of light polarization

Having the idea about the nature of light polarization, we can think about how to generate, examine and manipulate it to fit our needs. One important optical element is a polarizer which lets a specific polarization (parallel to the transmission axis) passes through while blocking others. There are many different types of polarizers. One kind is a parallel conducting wires grid. The light polarized parallel to the wires can drive the electrons along the wire. The accelerated electrons re-radiate in both forward and backward directions. The forward re-radiated wave tends to cancel the incident wave. Then backward re-radiated wave appears as a reflection. Besides, the accelerated electrons collide with lattice atoms, imparting energy to them and thereby heating the wires. On the contrary, the light polarized perpendicular to the

wires does not have such strong interaction with electrons. Thus, the transmission axis of the conducting wires is perpendicular to the orientation of the wires.

In 1938, Land invented the H-sheet, the so-called polaroid polarizer, probably the most widely used polarizer nowadays. It is made from polyvinyl alcohol (PVA) plastic with iodine doping. A sheet of PVA is heated and stretched in one direction. Then the sheet is dipped into an ink solution rich in iodine. A Polaroid polarizing filter functions similarly on an atomic scale to the wire-grid polarizer. The electrons associated with iodine can move along the chains as if they were long thin wires. Thus, the incident light polarized parallelly to the chains is absorbed (contrary to the metal wire-grid where the light is mostly reflected), while the light polarized perpendicularly to the chains is transmitted.

A dichroic crystal (like tourmaline), possessing an anisotropic crystalline structure, can also be made as a polarizer. There is a specific direction in the crystal known as the optical axis determined by the atomic configuration. The light polarization perpendicular to the optical axis is strongly absorbed. Note the absorption is usually wavelength-dependent. So, the crystal might appear colored when illuminated by natural white light. Even though one uses it for monochromatic light, the crystal must be thick enough to absorb the light completely.

Another type of polarizer made of birefringent crystals (typically calcite) is most commonly used with high-power lasers. In 1669, Erasmus Bartholinus observed a remarkable optical phenomenon in calcite, which he called double refraction. An incident ray of light is split into two rays, an ordinary ray (o-ray) and an extraordinary ray (e-ray). One type of birefringent polarizer is called the Glan-Foucault polarizer. The electric fields of the incoming ray are either completely parallel or perpendicular to the optical axis of a calcite crystal so that there is no difference between the o-ray and e-ray. The rays go through the crystal and reach the calcite-air interface with incident angle θ. If the incident angle meets the criteria $n_e < \frac{1}{sin\theta} < n_o$, then the o-ray, and not the e-ray, is internally reflected. The output consists of e-ray only, which is linearly polarized.

Ideally, if two polarizers are placed orthogonally oriented (crossed) in front of a light source, no light can pass through so that the intensity is equal to zero. According to Malus's law, published in 1809 by Etienne Malus, the intensity of transmitted radiance is dependent on the angle between transmission axes of two polarizers in the following way:

$$I = I_0 cos^2\theta \tag{1.4}$$

From this equation, the maximum intensity is obtained when θ = 0°, which means the two transmission axes are parallel to each other.

Another often used optical element for light polarization control and manipulation is a retarder (or a wave plate) constructed from a birefringent material. As discussed

above, an electric field of an electromagnetic wave can be expressed as a sum of two orthogonal components. The function of a retarder (a wave plate or a compensator) is to introduce a phase shift Δφ between the two perpendicular components that alter the output polarization.

The optical axis of a wave plate is parallel to both the front and back surfaces of the crystal (**Figure 1.3a**). The electric field of normal incident light can be split into two components that are parallel $E_{\parallel}$ and perpendicular $E_{\perp}$ to the optic axis. Since the speed of $E_{\parallel}$ is faster than $E_{\perp}$, the e-wave will move faster than the o-wave, resulting in a phase shift Δφ which is expressed as:

$$\Delta\phi = \frac{2\pi}{\lambda_0} d(|n_0 - n_e|) \tag{1.5}$$

where λ_0 is the wavelength in vacuum, and d is the thickness of the crystal. By changing the thickness, any desired phase shift Δφ can be obtained.

Compensators are another type of retarder (**Figure 1.3b**). Unlike wave plates, compensators are capable of introducing a controllable retardance on a wave. For example, the Berek compensator has its optic axis perpendicular to the surface of the plate. For normal incident light, the Berek compensator acts as an isotropic crystal. A phase shift can be obtained by tilting the crystal relative to the incident light. Therefore, the Berek compensator is a wave plate with varied retardance. It is worth mentioning that all these retarders are wavelength-dependent.

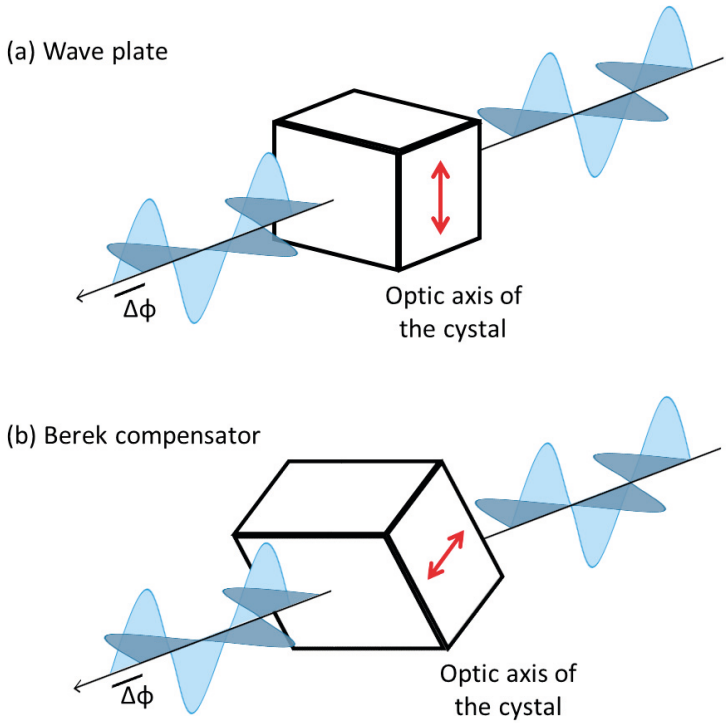

Figure 1.3. Schematic diagram of (a) wave plate and (b) Berek compensator.

1.1.3 Linear dichroism and fluorescence anisotropy

Intensity, wavelength, and polarization are the important properties of light. The degree to which different polarization components of light are absorbed/emit by an object yields valuable information about the nature of the interaction of the object with light.

Linear dichroism (LD) is the difference between the absorbance of light polarized parallel and perpendicular to the specific orientation axis of the sample, $LD(\lambda) = A_{\parallel}(\lambda) - A_{\perp}(\lambda)$. The LD measurements are designed to work with a sample for which the preferential orientation is known. From the LD measurement, one can learn the molecular structure or shape and investigate the interaction between molecules and their environment.[9–11] Wavelength-dependence of LD indicates that optical transitions of different energies involve molecular orbitals of different geometries having different orientations of the transition dipole moments relative to the structural axes of the molecule.[12,7] LD measurement is designed for ensembled samples with a known main axis of orientation. However, for single molecules or individual nanoobject which possess tiny absorption cross-section, fluorescence detected linear dichroism (FDLD) is a practical alternative.[13]

In contrast to linear dichroism, fluorescence emission anisotropy is used for characterizing the energy transfer process or molecule rotation of an isotropic sample. F.Weigert reported polarized emission from a dye solution for the first time in 1920.[14] From Malus law, the transition dipole moments parallel to the electric vector of the incident light can be excited more than the transition dipole moment orthogonal to the electric vector, which is called photoselection (**Figure 1.4**). The emission is measured by a polarizer placed between the sample and a detector. Fluorescence anisotropy (r) and the degree of polarization (P) are commonly used for quantitatively describing the emission polarization:

$$r = \frac{I_{\parallel} - I_{\perp}}{I_{\parallel} + 2I_{\perp}} \tag{1.6}$$

$$P = \frac{I_{\parallel} - I_{\perp}}{I_{\parallel} + I_{\perp}} \tag{1.7}$$

where $I_{\parallel}$ and $I_{\perp}$ are the electric vector of emission parallel and perpendicular to the electric vector of linearly polarized incident light (excitation light).

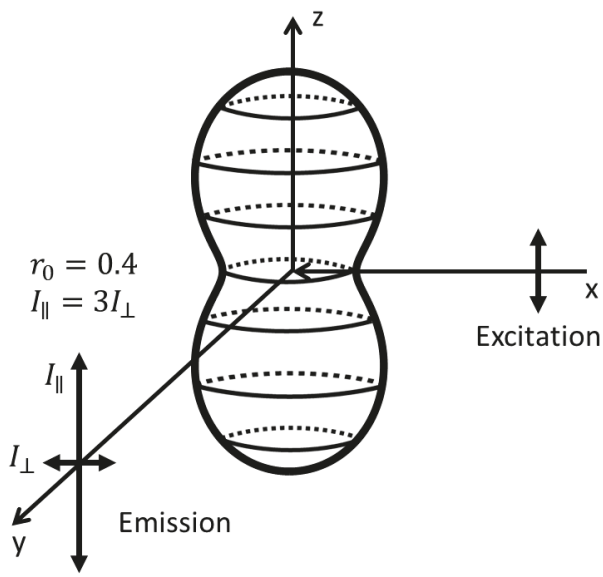

Figure 1.4. Excited-state distribution for immobile fluorophores with r_0 = 0.4.

1.2 π-conjugated systems

In the late 1970s, the field of organic semiconductors was significantly influenced by the discovery of poly(acetylene) doped by bromide or iodine vapors. The doped

polymers can achieve high conductivity. In 2000, the discovery and further development of these conductive polymers were rewarded with Nobel Prize in Chemistry to Hideki Shirakawa, Alan G. MacDiarmid, and Alan J. Heeger. In contrast to inorganic semiconductors, conjugated organic systems have high mechanical flexibility and low costs for production. Nowadays, organic semiconductors are widely used in light-emitting diodes, field-effect transistors, and solar cells. It is essential to study the fundamental optical and electronic properties of organic semiconductor materials to improve devices' efficiency and usability.

1.2.1 From atomic orbitals to molecular orbitals

An organic semiconductor is a carbon-based material. A π-conjugated system is a hydrocarbon chain with alternating single and double bonds, so-called conjugated double bonds. A carbon atom has four valence electrons $2s^2 2p^2$ which can generate three sp^2 orbitals on the molecule plane and one orthogonally oriented p_z orbital (**Figure 1.5b**). σ-bonds created by the overlap of sp^2 hold the molecule structure. π-bonds generated by the overlap of p_z orbitals result in electron delocalization, which is the origin of the properties that characterize conjugated polymers as semiconductors.

A molecule orbital may be approximated by a linear combination of atomic orbitals (LCAO).[15] The combination of two atoms orbitals leads to constructive (bonding) and destructive (anti-bonding, denoted with a star) interference of the two electrons' wavefunctions. The energy level associated with two ways of interference (**Figure 1.5a**) can be calculated from the Schrödinger equation. It turns out that the bonding state possesses lower energy than the anti-bonding state. And the splitting (ΔE) has the maximum value when the two interacting orbitals have the same energy.

For conjugated polymers, electrons occupy the lower energy π orbital – the highest occupied molecular orbital (HOMO), while the higher energy π* orbital is left unoccupied – the lowest unoccupied molecular orbital (LUMO).[16] A schematic band diagram and hybrid orbitals are shown in **Figure 1.5**. For most of the conjugated polymer, the bandgap between LUMO and HOMO is around 1.5 – 3 eV, which leads to the visible light absorption and emission.

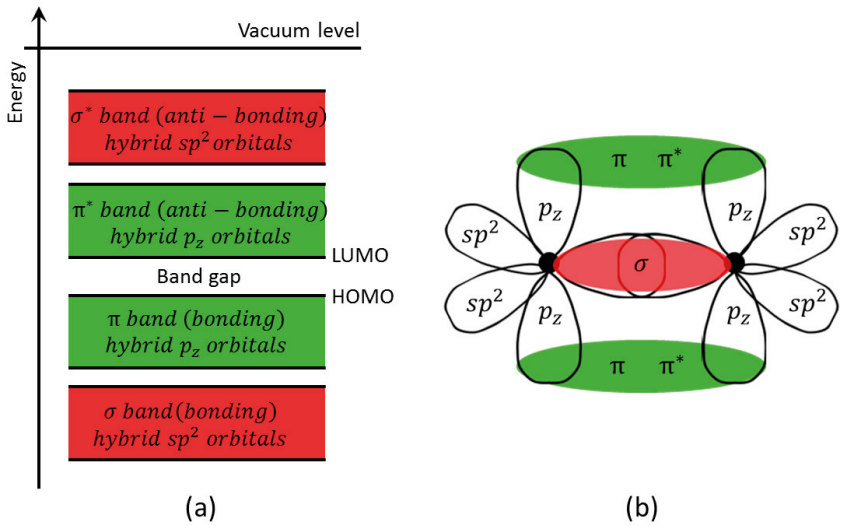

Figure 1.5. (a) Schematic band diagram for conjugated systems. (b) Atomic orbitals (sp^2 and p_z) and generated hybrid orbitals (σ-red, π-green) of carbons.

Electrons can be excited from HOMO to LUMO by absorbing enough energy of light. The rate of transition k_{if} between an initial state (i) and a final state (f) is expressed as:

$$k_{if} = \frac{2\pi}{\hbar}\rho\left|\langle\Psi_{el,f}|\hat{\mu}|\Psi_{el,i}\rangle\right|^2\left|\langle\Psi_{vib,f}|\Psi_{vib,i}\rangle\right|^2\left|\langle\Psi_{spin,f}|\Psi_{spin,i}\rangle\right|^2 \quad (1.8)$$

where Ψ_{el}, $\Psi_{vib,}$ and Ψ_{vib} are the electronic wavefunction, the vibrational wavefunction, and the spin wavefunction, respectively. $\hat{\mu}$ is the electric dipole operator. ρ is the density of final states. The vibrational wavefunction and the spin function are insensitive to the dipole operator so that they can be treated as constant factors. If any of these factors is zero, the transition is forbidden.[15] The molecular wavefunction is $\Psi = \Psi_{el}\Psi_{spin}\Psi_{vib}$, so **Eq. 1.8** can be written as $k_{if} = \frac{2\pi}{\hbar}\rho\left|\langle\Psi_f|\hat{\mu}|\Psi_i\rangle\right|^2$. The integral $\langle\Psi_f|\hat{\mu}|\Psi_i\rangle$ is so-called transition dipole moment (TDM).

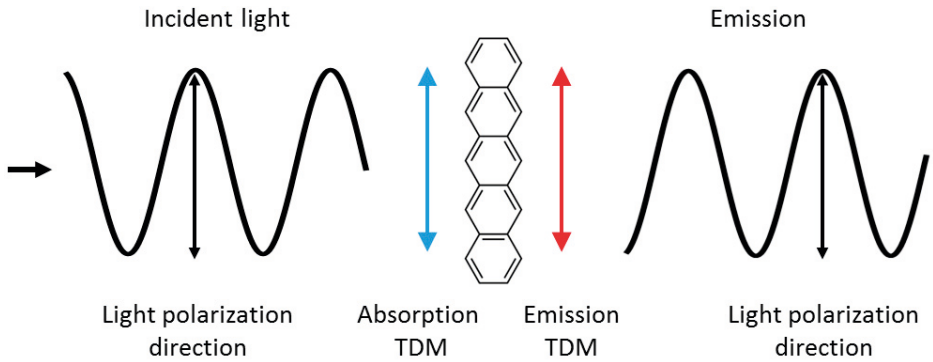

Figure 1.6. The absorption transition dipole moment (TDM) (blue double-headed arrow) and the emission TDM (red double-headed arrow) of the molecules are in the same direction. The electric field oscillation of the incident light is parallel to the TDMs of the molecule. In this case, the molecule absorbs and, as a consequence, emits the maximum amount of light.

Generally, the transition dipole moment of the π→ π* transition is directed along the backbone of molecules[17] (**Figure 1.6**). So, ordered polymer chains in a film have linear dichroism and fluorescence anisotropy, which means the polymer film absorbs or emits the maximum amount of light if it is polarized along with the main orientation of the polymer chains.

A polarized optical microscope is a common technique for studying oriented polymer chains. Note that due to the limit of optical resolution, the oriented domains need to be larger than the diffraction limit to observe the above effect. Otherwise, the polarization from differently oriented domains will be averaged within the optical resolution and shows no preferential absorption or emission.

1.2.2 Electronic coupling between molecules (H/J-aggregates)

The absorption and emission of one isolated chromophore can be affected by the environment due to electrostatic interactions with adjacent molecules.[15] Considering two chromophores as two point-dipoles with dipole moments p_1 and p_2, the interaction energy between them is given by:

$$V_{12} = \frac{1}{4\pi\varepsilon_0}\frac{p_1 p_2 - 3(p_1\hat{r})(p_2\hat{r})}{r^3} \tag{1.9}$$

where $\hat{r} = \vec{r}/r$ denotes the unit vector connecting the two dipoles. The equation shows that the orientation of the dipole moments and the distance between them affect the interaction energy V_{12}. Assuming that p_2 is the dipole moment induced in the adjacent molecule, then $p_2 = \alpha E_1$, where α is the polarizability of the adjacent molecule and $E_1 = 2p_1/4\pi\varepsilon_0 r^3$. Thus, the interaction energy increases with the polarizability α and the dipole moment p_1 of the molecule.

Here we consider the Coulomb interaction between two identical molecules, one in the ground state and another one in the excited state. This simple treatment is introduced by Michael Kasha.[18]

The ground state energy of the two-molecule system is obtained by solving the Schrödinger equation as:

$$E_g = E_1 + E_2 + D \tag{1.10}$$

where D is the electronic interaction in the ground state:

$$D = \langle \Psi_1 \Psi_2 | V_{12} | \Psi_1 \Psi_2 \rangle \tag{1.11}$$

where V_{12} takes the form of **eq. 1.9**. D is negative and corresponds to the van-der-Waals interaction energy. D lowers the ground state of the system of two molecules compared to the ground state energy of the individual molecules.

Now we consider the electronic interaction in the excited state. If one of the molecules becomes excited, the excitation can oscillate between the two molecules. The excited state wavefunction of the two-molecule system is a linear combination of both situations. This coupling can be either symmetric or anti-symmetric. Consequently, the excited state wavefunctions are:

$$\Psi_{E\pm} = \frac{1}{\sqrt{2}} (\Psi_1{}^* \Psi_2 \pm \Psi_1 \Psi_2{}^*) \tag{1.12}$$

Then Coulomb and resonance interaction can be expressed in the split energy level by solving Schrödinger equation:

$$E_{E+} = E_1^* + E_2 + D' + \beta \tag{1.13}$$

$$E_{E-} = E_1^* + E_2 + D' - \beta \tag{1.14}$$

where E_1* and E_2 are the energies of molecule 1 in the excited state and molecule 2 in the ground state, respectively. $D' = \langle \Psi_1{}^* \Psi_2 | V_{12} | \Psi_1{}^* \Psi_2 \rangle$ is the Coulomb interaction between molecule 1 in the excited state $\Psi_1{}^*$ and molecule 2 in the ground state Ψ_2. $\beta = \langle \Psi_1{}^* \Psi_2 | V_{12} | \Psi_1 \Psi_2{}^* \rangle$ is the resonance interaction that determines the splitting between the two levels E_{E+} and E_{E-}. The degree of β depends on the wavefunction overlap and is thus very sensitive to intermolecular distance.

The experimentally observed absorption or emission spectrum is the transition energy between the two-molecule system's ground and excited state:

$$\Delta E_{total} = (E_1^* + E_2 + D' \pm \beta) - (E_1 + E_2 + D) \tag{1.15}$$

$$= \Delta E_1 + \Delta D \pm \beta \tag{1.16}$$

It means the exciting energy of molecule 1 is shifted by the difference of polarization energy ΔD and resonance energy β.

The transition dipole moment for the coupled molecules is given by:

$$\mu_{\pm} = \langle \Psi_G | e\vec{r} | \Psi_{E\pm} \rangle \quad (1.17)$$

$$= \langle \Psi_1 \Psi_2 | e\vec{r} | \Psi_1{}^* \Psi_2 \pm \Psi_1 \Psi_2{}^* \rangle \quad (1.18)$$

$$= \frac{1}{\sqrt{2}} (\vec{\mu}_1 \pm \vec{\mu}_2) \quad (1.19)$$

where the transition dipole moments are $\mu_1 = \langle \Psi_1 | e\vec{r} | \Psi_1^* \rangle$, $\mu_2 = \langle \Psi_2 | e\vec{r} | \Psi_2^* \rangle$ for non-interacting molecules. The transition dipole moment of the coupled molecules results from the vector sum of the transition dipole moments of individual molecules.

H-type interaction (**Figure 1.7a**) occurs when the two molecules are arranged in a coplanar, stacked manner. The parallel arrangement possesses transition dipole moment 2μ, and the energy of this state is high (E_+). The transition from the ground state to the state of the anti-parallel arrangement (the lower energy level E_-) is forbidden due to zero dipole moment. A prominent example is the lutein solution investigated in detail by Zsila et al.

J-type interaction (**Figure 1.7b**) occurs when the two molecules are arranged in a co-linear manner. The lower energy state E_- possesses transition dipole moment 2μ due to the parallel sequence of transition dipole moment. The transition to the higher energy level E_+ (anti-parallel order) is forbidden due to the zero dipole moment vector.

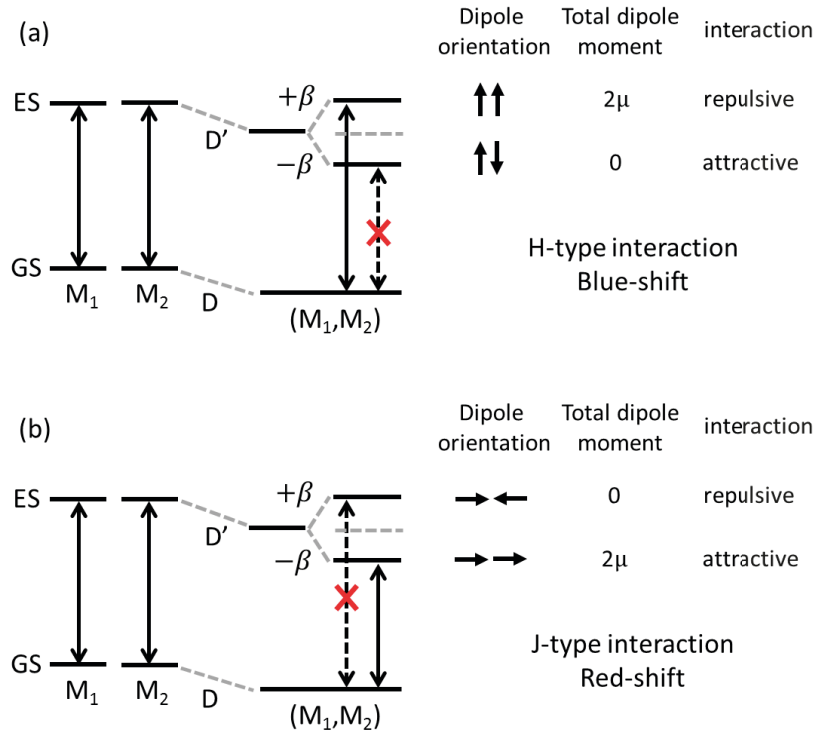

Figure 1.7. Schematic illustrating the effect of H-type (a) and J-type (b) electronic coupling of two molecules. GS and ES are ground state and excited state, respectively. D and D' represent Coulomb interaction/van-der-Waals interaction between M1 and M2. Furthermore, the excited state splits by resonance energy β into two levels. (a) H-type interaction (a side-by-side orientation). (b) J-type interaction (a head-to-tail orientation).

An advancement of Kasha's treatment is from the work of Spano and his co-workers.[19–22] They considered the coupling of the electronic dimer states to molecular vibrations and applied this to H- and J-type aggregates. The theory explains how the Franck-Condon progression of an isolated chromophore is distorted when the chromophore is embedded in an aggregate.[15]

Each vibronic level of S1 state splits into an exciton band, forming a set of vibrational sub-bands in analogy to the vibronic features in the isolated chromophore. If the bandwidth is less than the vibrational quantum $h\omega_0$, those bands are separated, and this refers to a weak exciton coupling, as shown in **Figure 1.8a and b**. If the bandwidth is larger than $h\omega_0$, those bands can superimpose and form a cumulative band which is the strong exciton coupling regime (**Figure 1.8 c and d**). The transitions shown in **Figure 1.8** are drawn in the condition of non-zero vibronic coupling. For example, if the coupling was zero, the monomer spectrum would consist only of a single line. This is because 0-1, 0-2 and so on transition would have zero Frank-Condon factors, and all transitions like 0-0, 1-1 and so on have the same energy.[23]

In H-aggregates, the chromophores are stacked in a side-by-side manner. The bottom of the bands is a $k = \pi$ states, and the tops are $k = 0$ states. Considering optical transition selection rule $\Delta k = 0$. Absorption and emission thus take place to and from the $k = 0$ states at the top of the band. Therefore, the absorption spectra of H-aggregates is blue shifted relative to the isolated chromophore. Excitons relax rapidly toward to the $k = \pi$ state of the S1 state. Ideally, for perfectly ordered H-aggregates at zero temperature without vibronic coupling, decay from $k = \pi$ state to the ground state is fully forbidden. In the case of vibronic coupling considered by Spano, the sidebands 0-1, 0-2, … appear, while the 0-0 transition remains forbidden. This happens because the coupling to phonons that carry momentum makes the bottom exciton state of the H-aggregates a mixture of the optically forbidden state ($k = \pi$) and optically allowed state k=0 state.

The situation is reversed in J-aggregates, in which the chromophores are aligned head-to-tail. The bottom of the bands is a $k = 0$ state and the top is $k = \pi$ state. Thus, absorption and emission occur to and from the $k = 0$ state at the bottom of the band, resulting in redshifted absorption and emission spectra in respect to isolated chromophores. The band-bottom exciton provides the origin for both absorption and emission. As a result, 0 – 0 absorption and emission peaks lie on top of each other. So ideally, there is no Stokes shift.

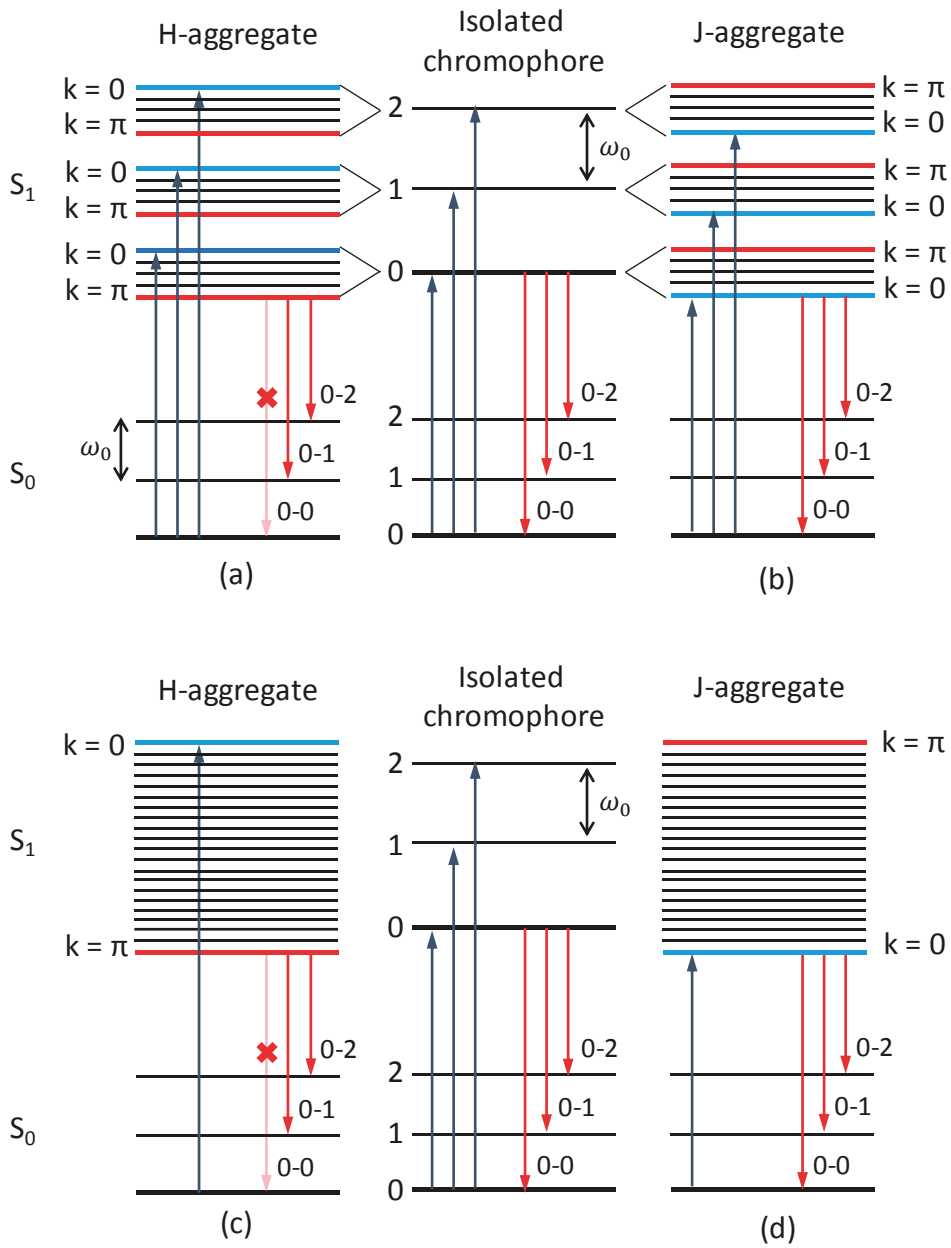

Figure 1.8. Approximate energy level diagrams in the case of vibronic coupling for the isolated chromophore (middle), H-aggregate (left) and J-aggregates (right). (a) weak exciton coupling and (b) strong exciton coupling. Blue energy levels are nodeless k = 0 exciton. Red energy levels are k = π excitons.

1.3 Perovskites

Lead-halide perovskites are crystals with a chemical formula ABX_3, where A (e.g., Cs^+ or $CH_3NH_3^+$) and B (Pb) are cations, and X is an anion (e.g., I, Br or Cl). The advantages of their photophysical properties, such as strong light absorption, long charge-carrier diffusion lengths, and low intrinsic surface recombination, make them a potential material for solar cell, light-emitting diode, photodetectors and lasers. Perovskite solar cell efficiency has increased from 3.8% in 2009 to 29.1% in 2020 (NREL efficiency chart),[24] exceeding the maximum efficiency achieved in single-junction silicon solar cells. Furthermore, absorption/emission polarization is one of the fundamental properties of photoactive materials, which has been applied in many modern technologies, such as optical antennas, 3D movies, or liquid crystal displays. In this section, we will focus on introducing the polarization-related study of perovskite materials. In this thesis, we mainly focus on $MAPbBr_3$ perovskite nano and microcrystals (**Figure 1.9**).

1.3.1 Electronic band structure

In solid-state, many atoms combine their electron density orbitals to form many energy splits. A large number of splits eventually forms continuous bands. The highest occupied band is called the valence band (VB), and the lowest unoccupied band is called the conduction band (CB). The energy gap between the valence band and conduction band is in the range from 0.5 eV to 3 eV. Taking $MAPbBr_3$ as an example, the major contributions to the conduction band and valence band are hybridized Pb(6p)-Br(4p) and Pb(6s)-Br(4p) orbitals (**Figure 1.10**).

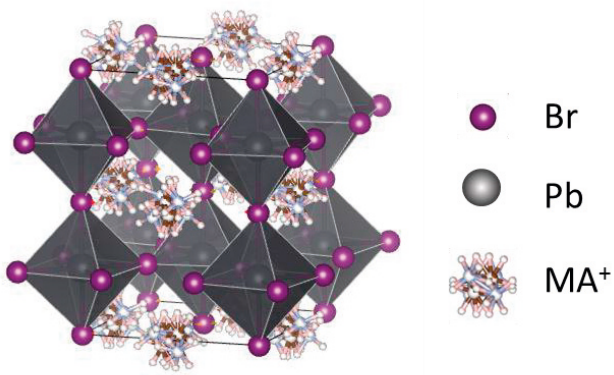

Figure 1.9. Crystal structure of $MAPbBr_3$.

An electron can jump to a conduction band under certain excitation. Meantime generate a hole in the valence band. An electron and a hole can be bounded by Coulombic interaction and form a so-called exciton. If binding energy is a few meV, the excitons are likely to be dissociated at room temperature. However, in some semiconductors and especially in low dimensional semiconductor structures (quantum dots, nanorods, or nanowires), the exciton binding energy is much higher and they can be the primary excited species even at room temperature.

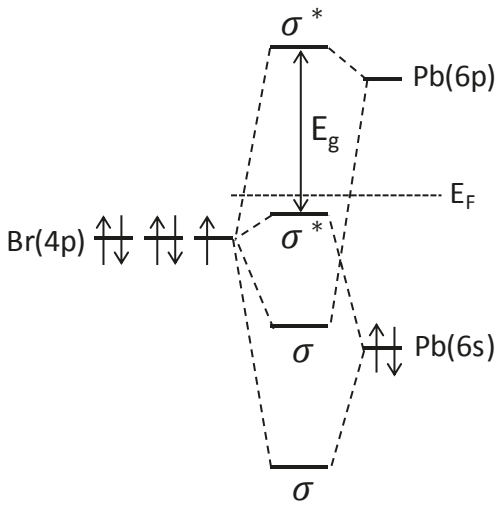

Figure 1.10. Schematic representation of sp hybridization in $MAPbBr_3$.

1.3.2 Dielectric screening effect

From the previous studies, light absorption/emission polarization in semiconductors may originate from the quantum confinement effect[25,26] dielectric contrast,[27,28] anisotropic TDMs induced by distortion of the crystal,[29] redistributions of charge near the interface,[30,31] or the combination of several of these factors. Here we are going to discuss in detail the energy splitting and the dielectric contrast induced polarization. This section focuses on explaining the absorption and emission polarization caused by dielectric contrast, the so-called dielectric screening effect.

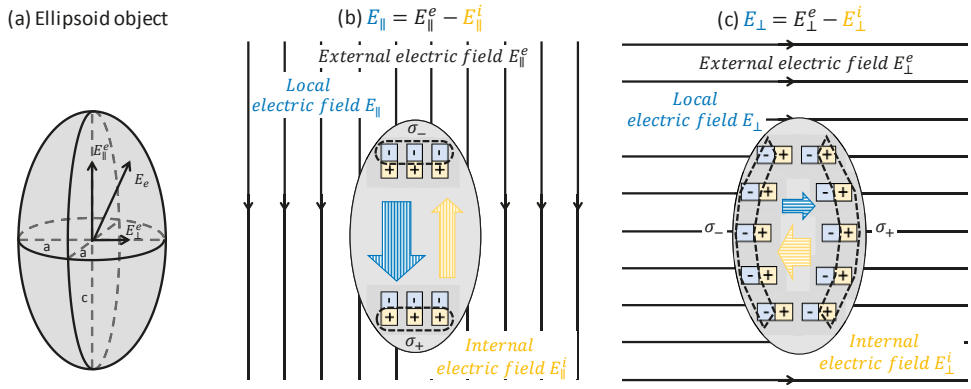

Figure 1.11. Ellipsoid used for illustrating dielectric screening effect. (a) The geometry of a prolate ellipsoid used for eq.1.20. E_0 is the external electric field projected on the long axis c ($E_{\parallel}^{e}$) and the short axis a ($E_{\perp}^{e}$). (b) The external electric field $E_{\parallel}^{e}$ is parallel to the major axis c. Charges accumulate on the surface of the object and generate the internal electric field $E_{\parallel}^{i}$ which has the direction opposite to $E_{\parallel}^{e}$. (c) The external electric field $E_{\perp}^{e}$ is perpendicular to the major axis c. Accumulated charges on the surface generate the internal electric field $E_{\perp}^{i}$, which also has the direction opposite to $E_{\perp}^{e}$. Due to the elongation of the geometry, $E_{\parallel}^{i} < E_{\perp}^{i}$ (yellow arrows), resulting in $E_{\parallel} > E_{\perp}$ (blue arrows) in eq. 1.20.

A difference in the dielectric constants of an elongated object and its surrounding medium (dielectric contrast) induces a difference in conditions for penetration of the external electric field oriented along with the object elongation and perpendicular to it (**Figure 1.11**). The positive charges σ_+ are displaced in the direction of the field and negative charges σ_- accumulate in the opposite direction. This creates an internal electric field E_i that reduces the overall field within the dielectric ellipsoid.

Taking an ellipsoid as an example, due to the anisotropic geometry of the object, the internal electric field $E_{\perp}^{i}$ perpendicular to the major axis strongly attenuates the external electric field $E_{\perp}^{e}$. In contrast, the internal electric field $E_{\parallel}^{i}$ parallel to the major axis is weaker and attenuates the external electric field less. The resultant local field $E_{\parallel} > E_{\perp}$ can be calculated by solving the Laplace equation resulting in the following results:[32]

$$E_{\parallel,\perp} = \frac{\varepsilon_0}{\varepsilon_0 + (\varepsilon - \varepsilon_0) n_{\parallel,\perp}} E_{\parallel,\perp}^{e} \tag{1.20}$$

where ε and ε_0 are the dielectric constants of the elongated object and its surrounding medium, respectively. $E_{\parallel}^{e}$ and $E_{\perp}^{e}$ are the projection of the external electric field E_e on the major and minor axis and $n_{\parallel,\perp}$ is the depolarization factor which depends on the semi-major axes (a,c) of the ellipsoid as

$$n_{\parallel} = \frac{1 - e^2}{2e^3}\left(ln\left(\frac{1+e}{1-e}\right) - 2e\right) \tag{1.21}$$

$$n_{\perp} = \frac{1 - n_{\parallel}}{2} \tag{1.22}$$

$$e = \sqrt{1 - a^2/c^2} \tag{1.23}$$

For an infinitely long ellipsoid (nanowire, a << c), $n_{\parallel}$ is close to 0 and $n_{\perp} = 0.5$. So $E_{\parallel} = E_e$ and $E_{\perp} = 2\varepsilon_0 E_e/(\varepsilon + \varepsilon_0)$.

From the above solution, one can calculate the polarization of absorption or PL. Note that we can use the static electric field model for absorption and PL because the object is much smaller than the excitation light wavelength so that the object can be seen as a dielectric material placed in a static electric field. Taking nanowire as an example, the ratio of absorption coefficient $k_{\parallel}/k_{\perp}$ and emission intensity $I_{\parallel}/I_{\perp}$ are:[27]

$$\frac{k_{\parallel}}{k_{\perp}} = \left|\frac{\varepsilon + \varepsilon_0}{2\varepsilon_0}\right|^2 \tag{1.24}$$

$$\frac{I_{\parallel}}{I_{\perp}} = \frac{(\varepsilon + \varepsilon_0)^2 + 2{\varepsilon_0}^2}{6{\varepsilon_0}^2} \tag{1.25}$$

1.4 Energy transfer

1.4.1 Förster resonance energy transfer

Förster resonance energy transfer (FRET) is a mechanism describing energy transfer between two light-sensitive molecules. FRET is a one-step process without the appearance of a photon or exchanging electrons (**Figure 1.6**). The excited state of donor D* is de-excited while the acceptor becomes excited from the ground to the excited state through a dipole-dipole interaction (**Figure 1.12a**):[15]

$$D^* + A \rightarrow D + A^* \tag{1.26}$$

The rate of energy transfer is calculated by:[7]

$$k_{ET} = \frac{9 \cdot ln10}{N_A} \frac{1}{2^7 \pi^5 n^4} \frac{Q_D}{\tau_D} \frac{\kappa^2}{R^6} \int I_D(\lambda) \varepsilon_A(\lambda) \lambda^4 d\lambda \tag{1.27}$$

where the Q_D is the quantum yield of a donor in the absence of an acceptor, τ_D is the lifetime of donor in the absence of acceptor, κ is the orientation factor and R is the distance between the donor and acceptor transition dipoles, N_A is Avogadro's number, n is the refractive index of the medium surrounding the donor and acceptor. The integral term $\int I_D(\lambda) \varepsilon_A(\lambda) \lambda^4 d\lambda$ expresses the extent of spectral overlap between the donor emission and acceptor absorption.

It is usually easier to think about the distance than the energy transfer rate, so the Förster distance R_0 can be defined as:

$$R_0 = \frac{9 \cdot ln10}{N_A} \frac{1}{2^7 \pi^5 n^4} Q_D \kappa^2 \int I_D(\lambda) \varepsilon_A(\lambda) \lambda^4 d\lambda \tag{1.28}$$

Combining with **eq. 1.27**, the energy transfer rate K_{ET} can be written as:

$$k_{ET} = \frac{1}{\tau_D^0} \left(\frac{R_0}{R}\right)^6 \tag{1.29}$$

The energy transfer efficiency ε is the ratio between energy transferred to another molecule and the total amount of absorbed energy:

$$\varepsilon = \frac{k_{ET}}{\tau_D^{-1} + k_{ET}} \tag{1.30}$$

This equation indicates that the high energy transfer efficiency can be obtained only when the energy transfer rate is faster than the lifetime of the excited state.

By recalling **eq.1.29**, the **eq. 1.30** can be rearranged as:

$$\varepsilon = \frac{{R_0}^6}{{R_0}^6 + R^6} \tag{1.31}$$

which shows the energy transfer efficiency is strongly dependent on the distance between donor and acceptor R. If R is equal to the Förster distance R_0, then half of the energy will transfer from donor to acceptor (**Figure 1.12b**).

In a short summary, Förster resonance energy transfer theory predicts that the K_{ET} depends on $1/R^6$, dipole orientation, spectra overlap, and excitation decay rate. The genius of Förster theory is that the equation is connected to spectra that can be measured experimentally.

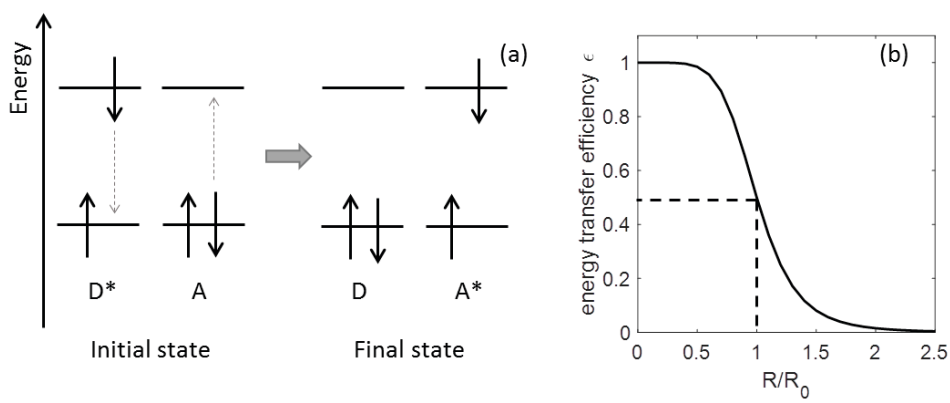

Figure 1.12. (a) Illustration of Förster resonance energy transfer. (b) Dependence of energy transfer efficiency on R/R_0.

It is worth noting that the point-dipole approximation limits the applicability of Förster theory. Thus, it may fail for conjugated polymer or oligomers, particularly for linear chromophores. It has been reported that the point-dipole approximation may under- and over-estimate the transfer rate for head-to-head and cofacial transition dipole configurations, respectively. [33]

1.4.2 Energy transfer in organic materials

π-conjugated polymer chains are examples of multichromophoric systems with energy transfer (ET). FRET can occur within a polymer chain (inter-chain ET) or between adjacent chains (intra-chain ET). The rate of ET depends on the chain conformation which can be controlled by the choice of solvent, polymer concentration, thermal annealing and substrates.[34,35] The time scales of ET range from picoseconds to nanoseconds.[36] Using ultrafast spectroscopy and quantum chemical calculations, it is shown that interchain ET is by a 1-order-of-magnitude larger than intrachain ET.[37] FRET is highly efficient if the donor and acceptor are positioned within the Förster radius (the distance at which half the excitation energy of the donor is transferred to the acceptor, typically 3 – 6 nm).[7]

The ET process in polymer chains is described below and shown in **Figure 1.13**. Due to the distortion or bend of polymer chains, one conjugation can be broken into several subunits (chromophores). Each unit possesses a different conjugation length. A longer conjugated unit has a lower bandgap. Subunits can absorb light and energy rapidly transfer to lower energy sites along the chain. Intrachain ET processes dominate in solution, while close contact between chains in films favors interchain ET transport.[38] For such a single multichromophoric object (e.g., an individual conjugated polymer chain), it is hard to measure the PL spectra of independent chromophores due to the diffraction limit. Hence, polarization measurement combining with single-molecule microscopy becomes a more efficient and necessary method.

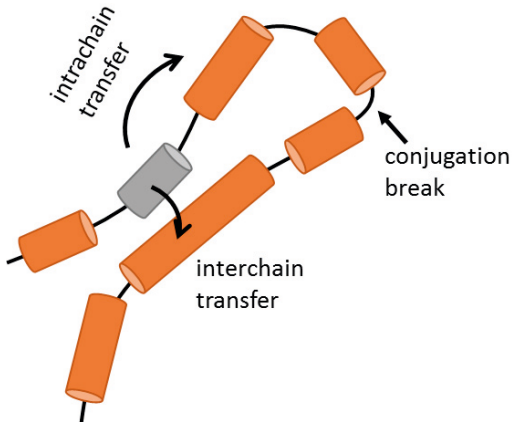

Figure 1.13. Schematic illustrates inter- and intra- chain FRET process. All the subunits absorb light. Energy tends to transfer from short conjugated unit to longer ones which have lower energy bandgap. The orange color represents stonger emission, and the gray color means weaker emission.

1.4.3 Energy transfer in aggregates

Semiconductor nanoparticles (NPs) exhibit unique optoelectronic properties due to their tiny size and the large surface-to-volume ratio. When the size of NPs is of the same magnitude as the de Broglie wavelength of the electron wave function, quantum confinement can be observed. As confining dimension decreases, the energy spectrum becomes discrete. As a result, the bandgap of NPs becomes size-dependent (**Figure 1.14**).

Förster resonance theory was first developed for the case of a single donor (e.g., a dye molecule) together with a single acceptor (e.g., a dye molecule). FRET in assembled nanostructure arrays, such as semiconductor nanoparticles (NPs), becomes more complicated.[39] Many groups proposed different models for the energy transfer process between nanocrystals by considering the confinement geometries, the assembly architectures, dielectric function,[40] the orientation of nanocrystals,[41] the nanoparticle stacking concentration[42] and so on. The FRET process in assembled nanocrystals systems can be affected by many factors so that the ET rate is more unpredictable.

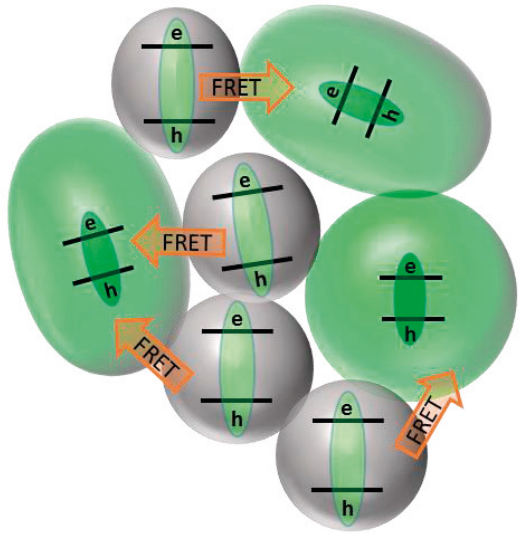

Figure 1.14. Proposed FRET process between nanoparticles within one aggregate. Due to the quantum confinement effect, smaller nanoparticles have a wider bandgap, while larger nanocrystals have a narrower bandgap. The excitation energy transfers from smaller nanocrystals to larger nanocrystals through dipole-dipole coupling.

1.4.4 Homo-FRET studied by fluorescence polarization

There are two different types of FRET, hetero-FRET and homo-FRET. Hetero-FRET refers to the cases when donor and acceptor molecules are spectroscopically different. The FRET rate of a blend conjugated polymer film can be studied from time-resolved and high-resolution spectroscopy because of the substantial energetic difference between the donor and acceptor.[43–45] If the energy transfer from a donor to an acceptor is efficient, it is expected to see that the PL intensity of blend film at the donor peak position is decreased. And the lifetime of the donor in blend film is shorter than the intrinsic donor film. With high time resolution, the acceptor's lifetime may rise within hundreds of picoseconds at the beginning due to receiving energy from the donor.[46]

However, the above methods become inefficient when donors and accepters are spectroscopically similar. Energy transfer in such systems is called homo-FRET. e.g., transfer between green fluorescent proteins.[47] Fluorescence anisotropy (FA) measurements is a powerful tool to investigate homo-FRET.[48–52] The parameter r_0 (calculated in **eq. 1.8**) can be used to estimate the energy transfer in an ensembled isotropic system, such as a solution. After the initial photoselection by linearly polarized excitation, r_0 is equal to 0.4 if no depolarization process (energy transfer

or rotation) occurs during the fluorescence lifetime. The r_0 will decreases if there are energy transfer processes and the minimum value of r_0 can reach to -0.2.

Some general polarization parameters, such as polarization P (calculated from **eq. 1.6**) and phase (θ, the angle of maximum absorption or emission), can also help us study the ET process within the system. Since energy transfer is a depolarization process, it leads that emission polarization (P_{em}, θ_{em}) is different from excitation polarization ($P_{ex,}$ θ_{ex}). In the later chapters, we assign the excitation and emission polarization P as excitation modulation depth (M_{ex}) and emission modulation depth (M_{em}), respectively.

Furthermore, even if the polarization properties of excitation and emission are the same, it is still possible that energy transfer occurs in the system. In this case, we will need a more advanced method to determine the ET process, the so-called single funnel model. More details can be found in Chapter 3. [53–55]

Chapter 2 Experimental methods

2.1 Fluorescence microscopy

Fluorescence microscopes use fluorescence to generate images and to study the properties of organic or inorganic substances. Epifluorescence microscope is widely used in scientific research. There are other advanced fluorescence microscopies based on the epifluorescence design, such as two-photon excitation microscopy, confocal microscopy, stimulated emission depletion microscopy (STED), super-resolution microscopy, etc. Our novel technique, two-dimensional polarization imaging (2D POLIM) which we will introduce later, is also based on epifluorescence microscopy.

The schematic diagram of the epifluorescence microscope is shown in **Figure 2.1**. This microscope can work for the sample possessing fluorescence such as dye molecules, π conjugated polymers, perovskite, and biological samples labelled with fluorescent stains. Fluorescence microscopy requires intense and near-monochromatic illumination, so lasers are the most widely used light source for fluorescence excitation. The dichroic mirror/beam splitter is the heart of a fluorescence microscope designed to reflect the laser to focus on the sample through the objective lens (**Figure 2.1**, blue line) and only transmit the fluorescence of the sample (**Figure 2.1**, red line) towards the detector. An extra excitation filter (clean-up filter) is placed in front of the dichroic mirror to ensure the excitation is monochromatic. Further, an extra emission filter (long pass or bandpass filter) is added to the emission path to ensure that the detector collects only the emission light with a specific wavelength range.

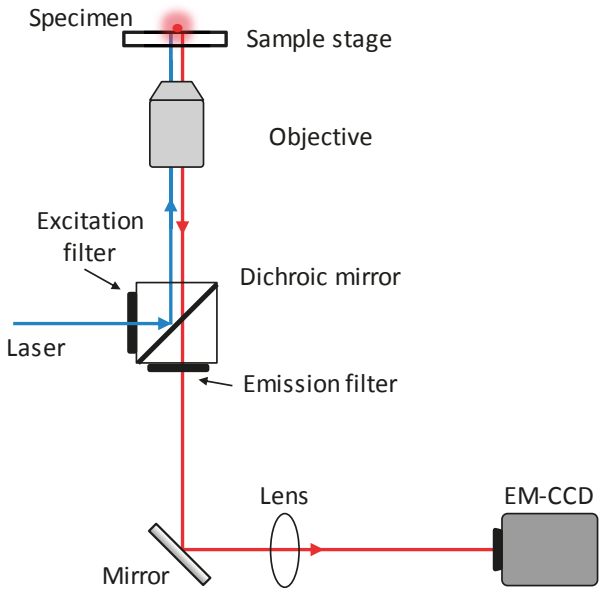

Figure 2.1. Schematic of an epifluorescence microscope

When light from a point source passes through the objective and projects on the chip of electron multiplying charge-coupled device (EM-CCD), the point appears as a small pattern (not a point), known as the Airy disk (**Figure 2.2a**). The radius R of Airy disk depends on the wavelength λ and the numerical aperture NA:

$$R = \frac{1.22\lambda}{2NA} \tag{2.1}$$

The distance R is also known as the effective resolution of a microscope. **Figure 2.2a** shows that if the two peaks are far away from each other, they can be easily recognized as separated objects. If the two peaks are separated by R (**Figure 2.2b**), the two emitters are just at the resolution limit of the optical system. This is the so-called Rayleigh criteria. As the separation is less than R (**Figure 2.2c**), one cannot distinguish the two peaks, and the objects are unresolved.

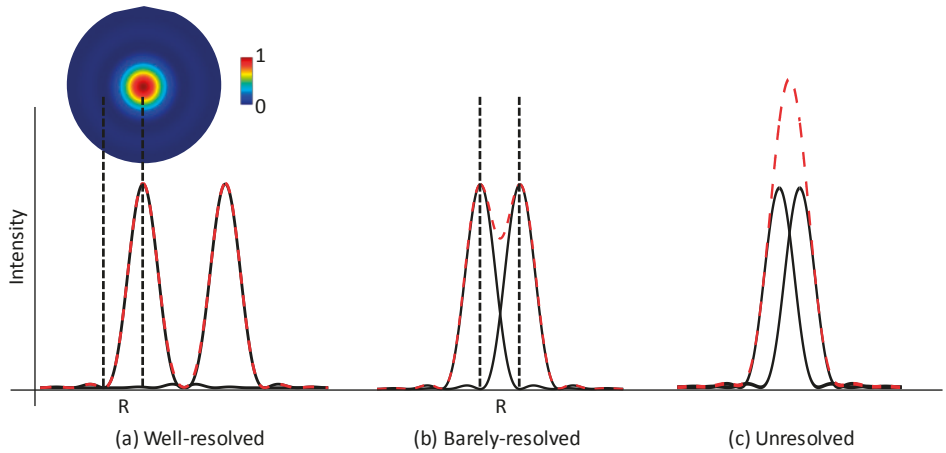

Figure 2.2. The relative displacement of Airy disks in 1D. (a) The spatial separation is >>R so that the two emitters are easily resolved. One plot of Airy disk. (b) The spatial separation is equal to R, so-called Rayleigh criterion. (c) The emitters are unresolved as they are within a distance of R.

2.2 Spectra measurement

To measure PL spectra, the signal passes through a slit and a holographic diffraction grating and is collected onto an EM-CCD camera (**Figure 2.3**). Such a scheme allows observing a sample image (zero-order of diffraction) and the spectra of the sample (first order of diffraction) simultaneously (**Figure 2.3**). Single molecules can be seen as a point light source, whereas in bulk material, the slit must be closed to avoid image overlap.

The spectral range is limited by the size of the chip in EM-CCD. Within this range, the EM-CCD is not equally sensitive to all wavelengths. Thus, the setup is further calibrated using a calibration tungsten incandescent lamp. Each pixel's effective size on the spectrum is about 3.23 nm, which is calculated from a mercury calibration lamp.

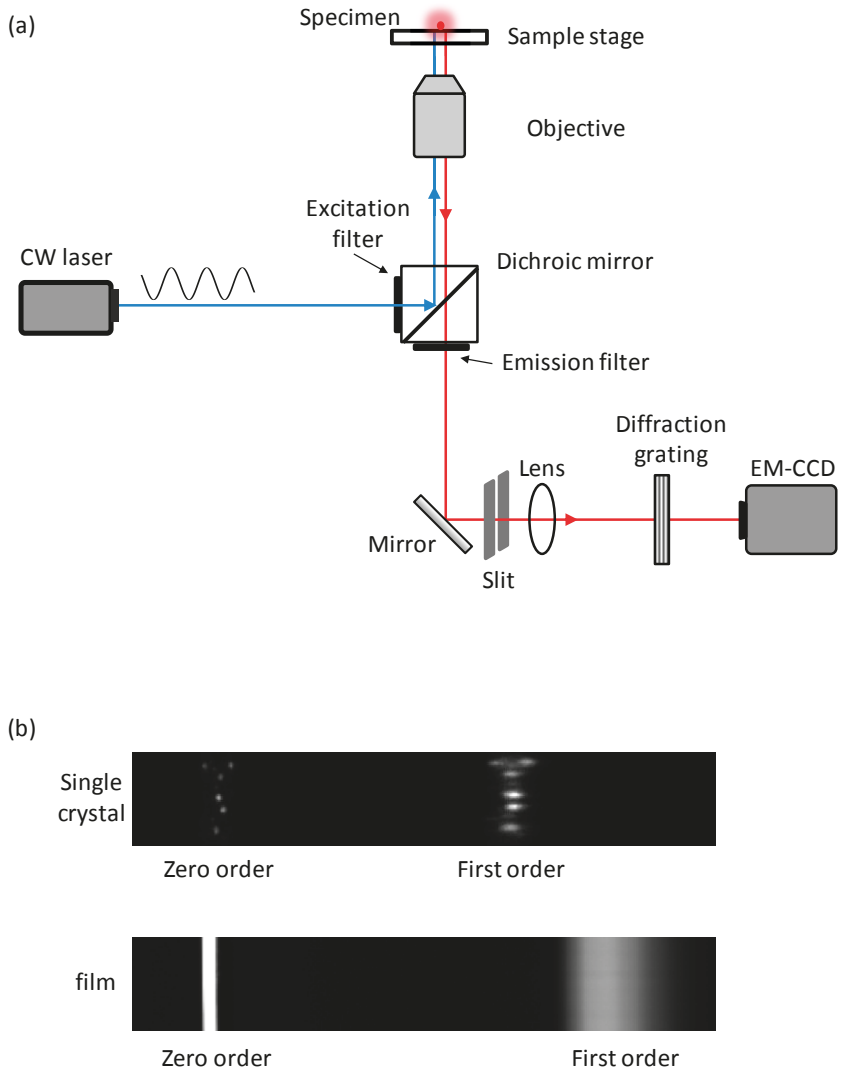

Figure 2.3. (a) Setup for fluorescence spectrum. (b) Experimental images of single $MAPbBr_3$ crystal (first row) and polymer (PBDT-TPD) film (second row). Both zero-order and first-order diffraction can be observed on the images.

2.3 Time correlated single-photon counting (TCSPC)

We used a pulsed laser, an avalanche photodiode (APD), and a time-correlated single-photon counting (TCSPC) to measure PL decay kinetics and calculate PL lifetime (**Figure 2.4**). A 50/50 beam splitter is inserted in front of EM-CCD. 50%

fluorescence will go to the EM-CCD used to image the sample plane. Another 50% light will be reflected by the beam splitter and collected by APD. A pinhole (100 μm in diameter) is placed in front of APD to block the light from the rest of the image. Together with the image on EM-CCD, one can locate the position of interest for the lifetime measurement. The smallest diameter of the area from which the signal can be collected using 40× Olympus LUCPlanFL, NA = 0.6 is about 1.2 μm.

TCSPC can be seen as a clock that can count the arrival time of a single photon compared to a reference signal directly from the light source. The clock is started by a START signal (from a sample) and stopped by another STOP signal (from reference light). Each START-STOP sequence is recorded and accumulated in a time channel (x-axis). The resulting histogram counts (y-axis) versus time channels (x-axis) represent the fluorescence intensity versus time.

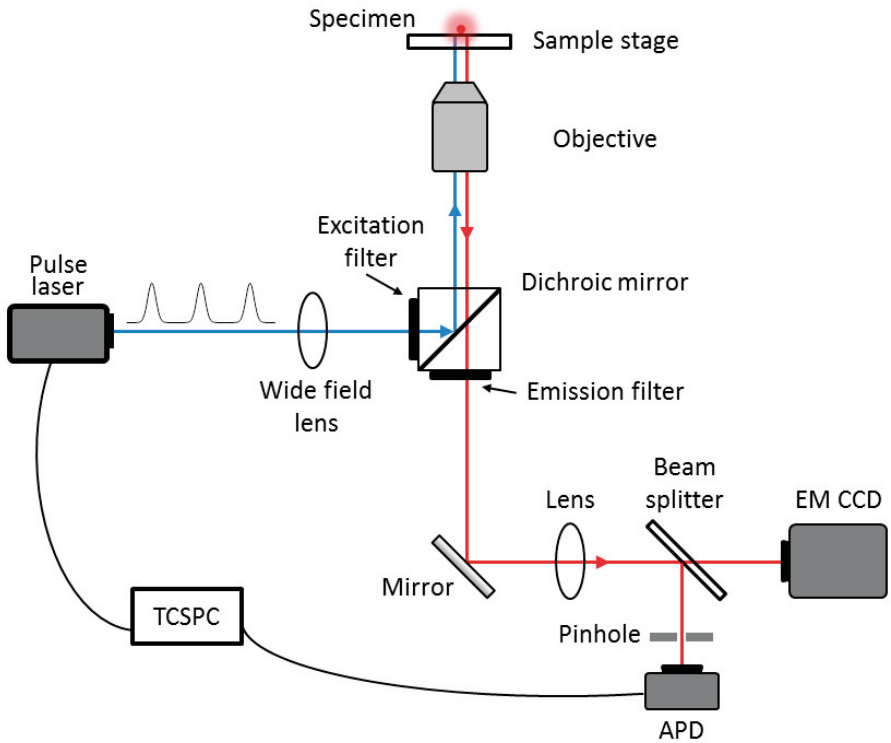

Figure 2.4. Setup to measure PL decay kinetics using time-correlated single photon counting (TCSPC).

2.4 Two-dimensional polarization imaging (2D POLIM)

2.4.1 Experimental setup

The setup for two-dimensional polarization imaging (2D POLIM) is shown in **Figure 2.5**. The main purpose of the setup is to experimentally determine the 2D function $I(\varphi_{ex}, \varphi_{em})$, the so-called 2D polarization portrait. 2D polarization portrait will be discussed later in Chapter 3.

2D POLIM setup is constructed on the basis of the wide-field epifluorescence microscope and several optical polarization elements ($\lambda/2$ plate, polarizer, and Berek compensator). The sample is excited by linearly polarized light. The orientation of the polarization plane can be set to any angle φ_{ex} by rotating the $\lambda/2$ plate. PL images are detected through an analyzer having the transmission axis at angle φ_{em}. All combinations of the angles are probed, giving the resulting 2D function $I(\varphi_{ex}, \varphi_{em})$.

The PL intensities $I(\varphi_{ex}, \varphi_{em})$ are generally recorded for six excitation angles (φ_{ex} = 0°, 30°, 60°, 90°, 120°, 150°) and four emission angles (φ_{em} = 0°, 45°, 90°, 135°). Consequently, 24 PL intensity images are collected by EM CCD camera. Theoretically, 24 combinations of angles are enough to construct one 2D portrait. However, we usually measure two rounds (48 images) in the actual measurement. The results from the second round can help us identify the data's reliability, especially for the single-molecule measurement. A home-built Labview program controls both the excitation controller and emission analyzer. So, the 24 images can be quickly obtained within two minutes.

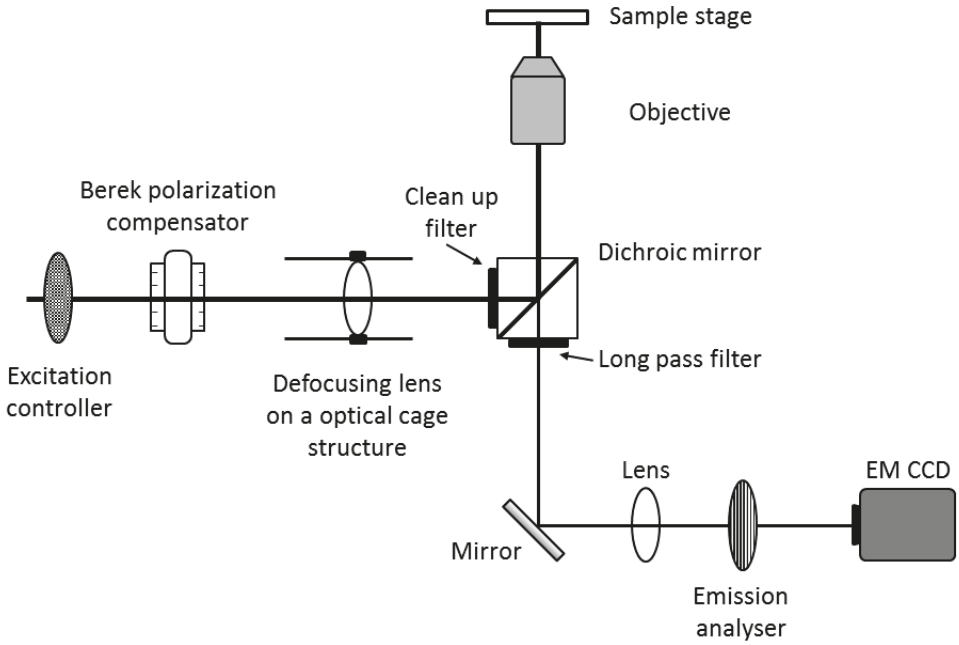

Figure 2.5. Two-dimensional polarization imaging (2D POLIM) setup. The excitation controller is a λ/2 plate mounted on a stepper motor, and the emission analyzer is a polarizer mounted on a stepper motor.

The acquired images can be analyzed in two different ways depending on the morphology of samples (**Figure 2.6**). In the pixel analysis (**Figure 2.6a**), the signals used to construct a 2D portrait are from each pixel. This data processing method is suitable for the sample possessing spatially homogeneous emission, such as a film. In the so-called single object analysis (**Figure 2.6b**), the signal is averaged over all the pixels representing an individual object. This is the case for a sample containing nanocrystals which appear as individual diffraction-limited spots at the image.

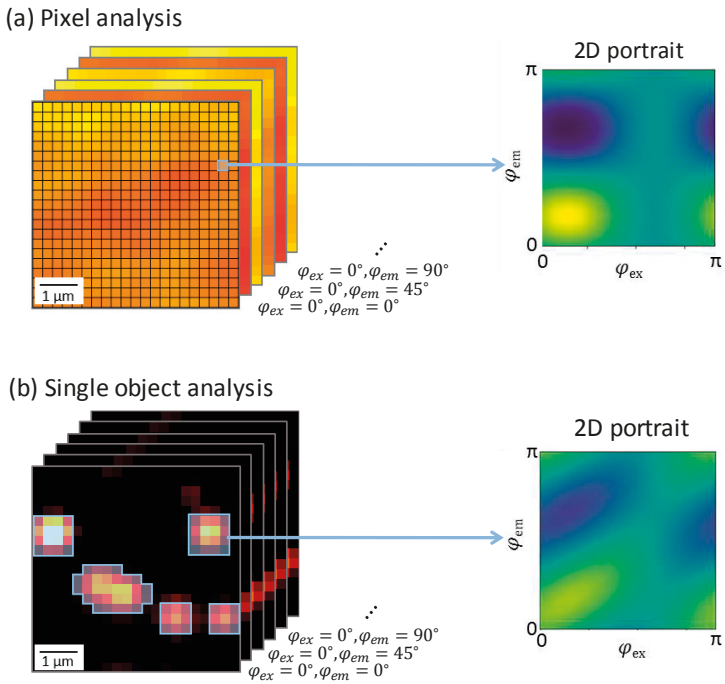

Figure 2.6. (a) Pixel analysis and (b) single object analysis of original PL intensity images.

2.4.2 Correction and characterization of polarization in 2D POLIM

The experimental scheme of 2D POLIM does not look too complicated. However, polarization artifacts induced from transmission-reflectance (Fresnel equations) and the birefringence can strongly affect the accuracy of the measurements. Thus, we need to have a correction routine for the setup.

A linearly polarized light can be considered as a linear combination of s- and p-polarized components (Chapter 1.1.1). According to Fresnel's equation, these two components transmit to a different extent. Consequently, i) the polarization orientation of transmitted light can be different from the incident light, and ii) the intensity of transmitted light is dependent on the polarization orientation of the incident light. Such an effect can be induced if optical elements (e.g., filters, mirrors) are not perpendicular to the light propagation.

Birefringent effect (Chapter 1.1.2) can also induce artifacts to experiment. When a light goes through a birefringent material, the component parallel to the optic axis has a different velocity than the perpendicular component. Thus, there is a phase retardation between these two components. Some of the optical elements are expectedly birefringent, acting as a λ/x waveplate. Practically, x is unknown.

Additionally, these effects are wavelength-dependent. Thus, the artifacts induced by birefringent are also tricky to be characterized and correct.

Practically, to obtain accurate experiment results, there are many factors that need to be considered:

i) The linearly polarized light at different angles should have constant intensity when they reach the sample plane.

ii) Optical elements, especially dichroic mirrors, can depolarize the excitation linearly polarized light due to the transmission and birefringence.

iii) For similar reasons, optics could also change the emission polarization.

iv) Interference pattern in excitation can also introduce error, especially for single-molecule measurements.

Based on the above concerns, we investigate how to characterize and correct the polarization artifacts in the 2D POLIM setup. It will be discussed in the following sections.

1. Polarization artifact in excitation – adjustment of Berek compensator

To ensure the accuracy of excitation polarization measurements, we need to be sure that: i) the polarization state of excitation light at the sample plane is linearly polarized, ii) The orientation of the excitation electric vector is precisely at the set angle, iii) To perform a 2D polarization measurement, the intensities at each angle need to be constant.

Berek compensator plays a vital role in overcoming the polarization artifact in excitation. A dichroic mirror in the cube of a microscope can introduce a significant depolarization effect from practical experience. By adjusting the retardation and orientation, the Berek compensator can behave as any wave plate (λ/x) to compensate the polarization artifacts which are introduced by dichroic mirror or other optical elements.

In our measurement, we use model 5540 Berek polarization compensator. This Berek compensator can impose ¼ or ½ retardance at any wavelength from 200 nm to 1600 nm. The retardance and the orientation of the plane can be adjusted conveniently and independently using two knurled rings. Precision scales allow us to set both tilt and orientation angles accurately. To a good approximation, the tilt angle θ_R gives retardance R (in waves):

$$\theta_R = sin^{-1}\left(0.284\sqrt{\lambda R}\right) \tag{2.2}$$

where λ is the wavelength in microns. The scales on retardation indicator is related to the tilt angle by:

$$I = 50.22 - 71sin\left(\frac{\pi}{4} - \theta_R\right) \quad (2.3)$$

It seems that one can easily set the Berek compensator to fulfill their requirement according to the above equations.

However, the challenge of adjusting the Berek compensator is that the microscope does not act as a waveplate due to the polarization-dependent transmittance-reflectance and birefringence. So the artifact induced by the microscope cannot be entirely compensated by a Berek compensator. Because of this, it is challenging to find retardation and orientation that can work for all angles.

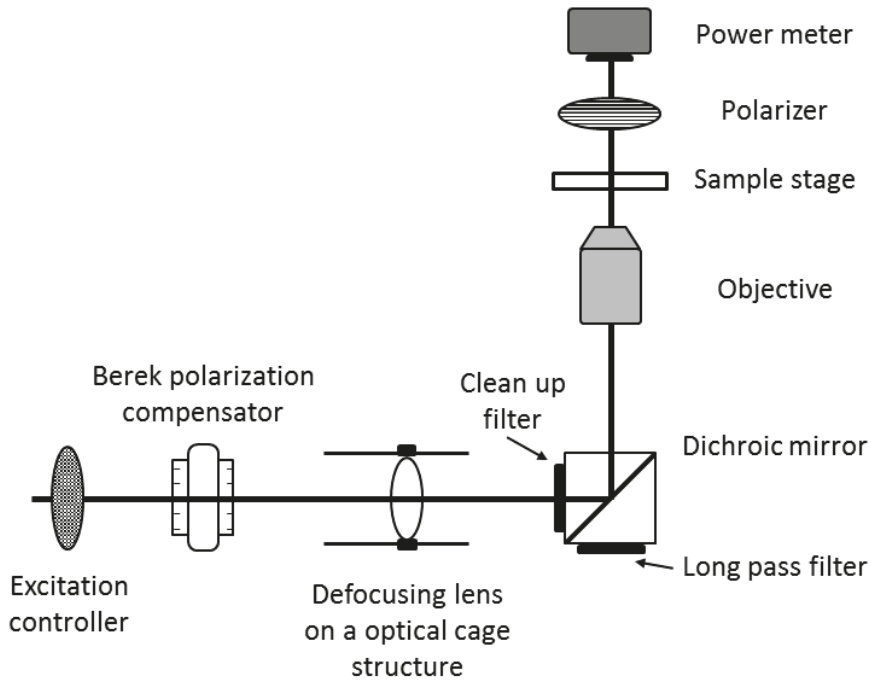

Figure 2.7. Experimental scheme for adjusting Berek polarization compensator.

To accurately find such a position, we design an experimental scheme as shown in **Figure 2.7** and use the following method. Instead of a sample, a polarizer is placed above the sample stage. The polarizer is continuously rotating. A power meter is used to measure the laser intensity after going through the polarizer. If it is pure linearly polarized light, the intensity will be a $\cos^2(\varphi_{polarizer})$ with a rotating polarizer and modulation depth $M = (I_{max}-I_{min})/(I_{max}+I_{min}) = 1$. The power meter is controlled by a Labview program so that it can calculate the value M in real-time. The ideal experiment condition is that M for all excitation angles is equal to1.

The excitation angle is fixed at 0° by the excitation controller and the polarizer above the sample stage is rotating. Meantime we adjust the Berek compensator and record all the positions of retardation and orientation when we are able to reach M > 0.95. Then we change the excitation angle to 30°, 60°, 90°, 120°, 150°, respectively and repeat the above steps. Finally, the position of the Berek compensator is chosen in such a way that M > 0.95 for all excitation angles used. In a similar experimental scheme but removing the polarizer, one can use a power meter to measure the power of the laser.

2. Polarization artifact in emission – isotropic emitter

It is also important that the polarization state of PL is not changed on its way from the sample to the detector. However, polarization artifacts also exist in the emission path similar to in excitation. The emission situation is even more complicated to deal with than for excitation because fluorescence is not monochromatic. Thus, the Berek compensator cannot be used for correction.

To correct the polarization artifact in emission, we measure the polarization property of an isotropic emitter. Theoretically, modulation depth (M_{em}^{iso}) should be equal to 0 for an isotropic emitter. However, in real measurements, M_{em}^{iso} is around 0.05 for 488 nm excitation due to the birefringence and transmittance artifact. A correction function (C_{em}) calculated from the experimental value M_{em}^{iso} and θ_{em}^{iso}:

$$C_{em}(\varphi_{em}) = 1 + M_{em}^{iso}\, cos\big(2\big[\varphi_{em} - \theta_{em}^{iso}\big]\big) \tag{2.4}$$

Thus, the intensity I can be corrected using the following equation:

$$I_C(\varphi_{ex}, \varphi_{em}) = \frac{I(\varphi_{ex}, \varphi_{em})}{C_{em}(\varphi_{em})} \tag{2.5}$$

3. Characterization of the accuracy of 2D POLIM – artificial molecule

In order to test the accuracy of the 2D POLIM measurement, we designed a so-called 'artificial molecule' (AM). The construction of AM is shown in **Figure 2.8**. The AM consists of a polarizer mounted on the rotation stage with a bottle of dye molecule solution placed on its top. The incident light passes through a polarizer and then absorbed by the solution, so the absorption of AM is linearly polarized. The emission from the dye molecule solution will pass through the same polarizer again, so the emission is also linearly polarized and has the same orientation of the absorption. The absorption and emission intensity depend on the orientation of AM as a $\cos^2$ function, which is the same as for a dipole. (**Figure 2.8b**).

We can change the orientation of the axis of the AM on the lab axis by rotating the polarizer. Ideally, for artificial molecule, $M_{ex}^{AM} = M_{em}^{AM} = 1$, $\theta_{ex}^{AM} = \theta_{em}^{AM} =$

$\Psi_{polarizer}$, where $\Psi_{\text{polarizer}}$ is the orientation of the AM. Luminescence shift (LS = $\theta_{em}^{AM} - \theta_{ex}^{AM}$), phase difference between excitation and emission, is equal to zero.

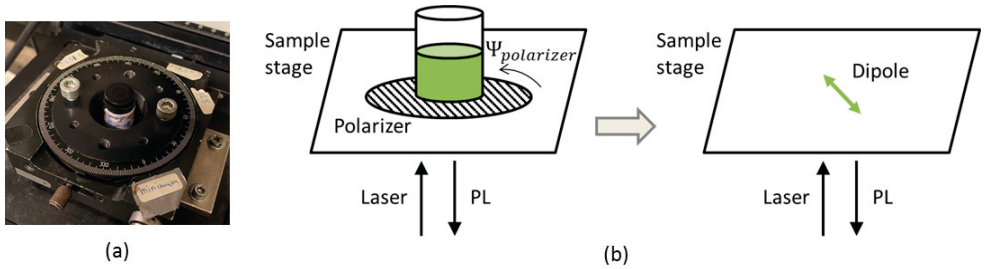

Figure 2.8. (a) A photograph and (b) a schematic diagram of the artificial molecule (AM). A bottle of isotropic solution placed on the top of a polarizer plays a role as a single dipole with a known orientation.

The polarization properties of the AM measured on the 2D POLIM setup are shown in the following table. For excitation at 488 nm, $0.96 \leq M_{ex} \leq 0.99$ and $0.93 \leq M_{em} \leq 0.98$. Mem can be further corrected by the method mentioned in section 2 so that $0.95 \leq M_{em} \leq 0.99$. The phase uncertainty is about one degree.

Table 2.1. Modulation depths, phases and LS of the AM oriented at 0°, 30°, 60°, 90°.

	M_{ex}	M_{em}	θ_{ex}	θ_{em}	LS
AM 0°	0.99	0.98	1	1	0
AM 30°	0.96	0.93	31	32	-1
AM 60°	0.97	0.95	62	63	-1
AM 90°	0.98	0.98	89	89	0

Chapter 3 Two-dimensional polarization imaging

3.1 Polarization portrait

Polarization portrait (**Figure 3.1**) is obtained by 2D POLIM measurement as described in Chapter 2. The sample is excited by linearly polarized light with the polarization plane oriented at angle φ_{ex}, and there is a polarizer in the emission path to detect the fluorescence intensity through an analyzer oriented at angle φ_{em}. Then for each pixel of the camera or for each selected object (**Figure 2.6**), we obtain a two-dimensional map of emission intensity $I(\varphi_{ex}, \varphi_{em})$ which we call polarization portrait. Compared with the traditional one-dimension method (when only one of the two angles is changed), the 2D polarization portrait contains a correlation between excitation and emission polarization properties which reflect the energy transfer process in the system.

How many angles do we need to measure to determine a polarization portrait unambiguously? According to the Malus law (Chapter 1), each cross-section of the function $I(\varphi_{ex}, \varphi_{em})$ at a fixed excitation angle φ_{ex} or emission angle φ_{em} has the functional form: $A \cos2(\varphi - \theta) + B$, where A, B, and θ are constants. Thus, the one-dimensional measurement has three degrees of freedom, which means we need three different combinations $(\varphi_{ex}, \varphi_{em})$ to calculate A, B, and θ. Consequently, at least nine different combinations $(\varphi_{ex}, \varphi_{em})$ are needed to determine such a two-dimensional portrait. Practically, to experimentally obtain more stable and accurate results, we measure 24 combinations of excitation angles (0°, 30°, 60°, 90°, 120°, 150°) and emission angles (0°, 45°, 90°, 135°), as mentioned in Chapter 2.4.

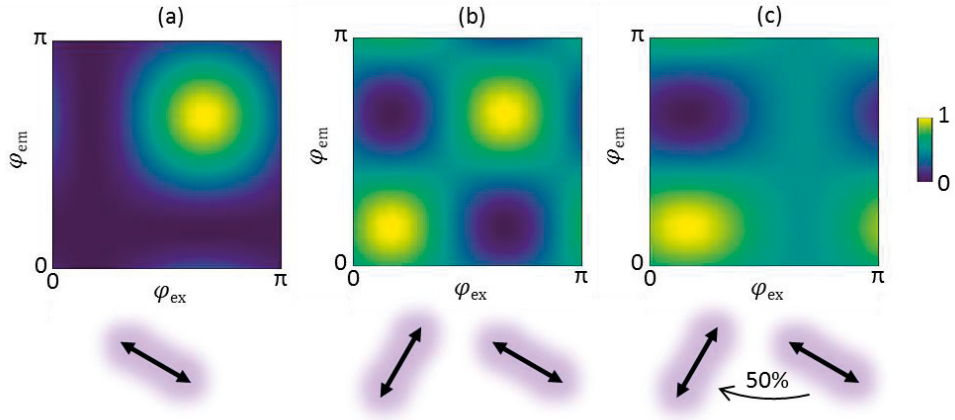

Figure 3.1. Examples of 2D polarization portraits. (a) one dipole oriented at 120°, (b) two dipoles oriented at 30° and 120° without energy transfer, (c) two dipoles oriented at 30° and 120°, 50% energy transfer of the dipole oriented at 120° transfers to the dipole oriented at 30°.

Figure 3.1 shows some examples which can help us to understand the meaning of patterns in polarization portraits. For one dipole (**Figure 3.1a**) oriented at 120°, only one yellow spot is located on the diagonal $\varphi_{ex} = \varphi_{em} = 120°$ corresponding to the maximum intensity of excitation and emission. By rotating the dipole, the location of the yellow circle moves along the diagonal. If two dipoles orient at different angles (**Figure 3.1b**) and no energy transfer (ET) between them, one can see two yellow spots, and the whole portrait is still symmetric relative to the diagonal. However, if there is energy transfer between two dipoles, the portrait's symmetry breaks, as shown in **Figure 3.1c**. What kind of quantitative information we can obtain from polarization portraits will be discussed in the following sections.

3.2 Polarization parameters

A polarization portrait contains information about the polarization properties of the system in both excitation and emission. One can extract some of this information directly from the portrait without any pre-knowledge of the system. For example, we can calculate polarization modulation depths, phases, and luminescence shifts by integrating along x-axis or y-axis of one 2D portrait. Experimentally. these parameters can also be measured from 1D polarization measurements.

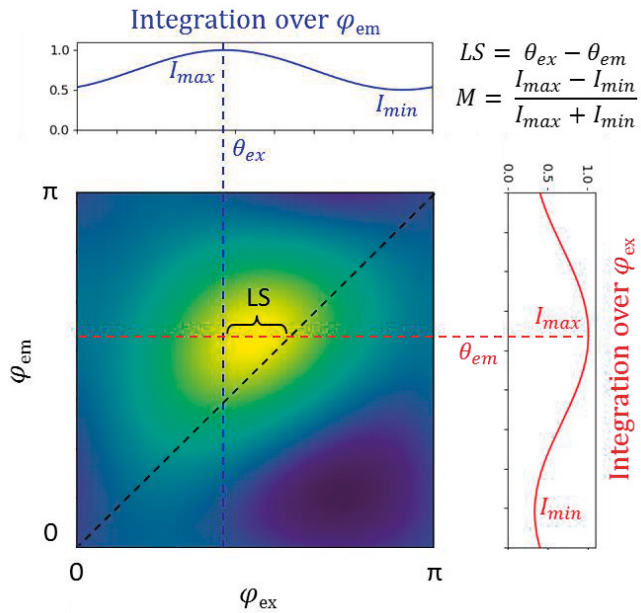

Figure 3.2. Visualization of the polarization parameters (modulation depth, phase and luminescence shift) extracted from polarization portrait.

The excitation polarization curve $I(\varphi_{ex})$ (**Figure 3.2**, the blue curve on the top) is obtained by integrating the portrait $I(\varphi_{ex}, \varphi_{em})$ over the emission angle φ_{em}. This curve can also be measured experimentally by exciting the sample with linearly polarized light at different angles and detecting emission without the analyzer. The I_{ex} has the following functional form according to the Malus law:

$$I_{ex}(\varphi_{ex}) = Acos^2(\varphi_{ex} - \theta) + B \tag{3.1}$$

where A, B and θ are constants. We can write the above equation in terms of maximum intensity I_{max} and minimum intensity I_{min} using some simple re-arrangements:

$$I_{max} = A + B \tag{3.2}$$

$$I_{min} = B \tag{3.3}$$

$$Acos^2(\varphi_{ex} - \theta) + B = (I_{max} - I_{min})cos^2(\varphi_{ex} - \theta) + I_{min} \tag{3.4}$$

Using the cosine half-angle formula, the above equation can be written as:

$$(I_{max} - I_{min})cos^2(\varphi_{ex} - \theta_{ex}) + I_{min}$$
$$= \frac{I_{max} + I_{min}}{2}\left[\frac{I_{max} - I_{min}}{I_{max} + I_{min}}\cos(2[\varphi_{ex} - \theta_{ex}]) + 1\right] \tag{3.5}$$

From **eq. 3.5**, we define three important polarization parameters: average intensity $\bar{I}$, excitation modulation depth M_{ex}, excitation phase θ_{ex}:

$$\bar{I} = \frac{I_{max} + I_{min}}{2} \tag{3.6}$$

$$M_{ex} = \frac{I_{max} - I_{min}}{I_{max} + I_{min}} \tag{3.7}$$

Thus **eq. 3.5** can be rewritten as:

$$I_{ex}(\varphi_{ex}) = \bar{I}[M_{ex}\cos(2[\varphi_{ex} - \theta_{ex}]) + 1] \tag{3.8}$$

The average intensity can also be obtained by exciting the sample with circularly polarized light and detecting the fluorescence without an analyzer. M_{ex} ranges from 0 to 1. For isotropic absorbers, such as randomly entangled conjugated polymer chains or a spin-cast dye molecules film, M_{ex} is equal to zero. If the excitation light polarization orients at the angle θ_{ex}, absorption of the excitation light is maximal. We define θ_{ex} as the excitation phase.

Similarly for emission, integration over the excitation polarization angle φ_{ex} yields the emission curve $I(\varphi_{em})$ (**Figure 3.2**, red curve on the right), and the same functional form can be written as:

$$I_{em}(\varphi_{em}) = \bar{I}[M_{em}\cos(2[\varphi_{em} - \theta_{em}]) + 1] \tag{3.9}$$

Where M_{em} and θ_{em} are emission modulation depth and phase, respectively. M_{em} ranges from 0 (an isotropic emitter) to 1 (a single dipole emitter). When the emission is measured through an analyzer, the signal reaches the maximum when the analyzer is set at the angle θ_{em}. Luminescence shift (LS) is the difference between the excitation and emission phases.

3.3 Energy transfer determination from polarization portrait

Excitation energy transfer is typical processes in a multi-chromophore system. Polarization is sensitive to the energy transfer because energy transfer leads to emission from chromophores which have a different orientation of the transition dipole moment than the originally excited chromophores. There are several ways to visualize the energy transfer process from a two-dimensional polarization portrait. We can measure fluorescence anisotropy, analyze a modulation depth correlation plot and a phase correlation plot and calculate the energy funneling efficiency.

3.3.1 Fluorescence anisotropy

As we mentioned in Chapter 1, fluorescence anisotropy is originated from the photoselection of randomly oriented molecules excited by linearly polarized excitation light. Photoselection means there is preferential excitation of chromophores oriented along the electric vector.

After the initial photoselection by linearly polarized excitation, if no reorientation of the dipoles and no energy transfer between them, then r is equal to fundamental emission anisotropy r_0. For dipoles randomly orient in a three-dimension (3D) space:

$$r_0 = \frac{2}{5}\left(\frac{3cos^2\beta - 1}{2}\right) \tag{3.10}$$

For dipoles randomly orient in a two-dimension (2D) plane:

$$r_0 = \frac{cos\,(2\beta)}{3 - 0.5cos\,(2\beta)} \tag{3.11}$$

where, β is the angle between the absorption and emission transitions. The angle β results in a further loss of anisotropy. In the absence of depolarizing processes (energy transfer or rotational diffusion), r_0 reached the maximum value of 0.4 (for both 3D and 2D) if a molecule possesses β = 0. In the case of 3D, r_0 is equal to zero when β = 54.7°, so-called magic angle. The minimum r_0 is -0.2 when β = 90°. In the case of 2D plane, r_0 is equal to zero when β = 45°. The minimum r_0 is -2/7 when β = 90°.

Fluorescence anisotropy can be seen from the polarization portrait, as shown in **Figure 3.3**. The higher intensity (**Figure 3.3 a**) on the diagonal is caused by photoselection. The portrait becomes flat (**Figure 3.3 b**) in the presence of depolarization processes. The fluorescence anisotropy can also be calculated from 2D portrait. By fixing an excitation angle φ_{ex}, $I_{\parallel} = I(\varphi_{ex}, \varphi_{ex})$, and $I_{\perp} = I(\varphi_{ex}, \varphi_{ex} + 90°)$. Then r can be calculated from **eq. 1.6**.

Note that for an isotropic sample, fluorescence anisotropy is independent of the excitation. Thus, one can use r as a parameter to quantify depolarization due to energy transfer or rotational diffusion. However, for an anisotropic system, such as an individual multi-chromophoric system, r varies with the excitation angle. Thus, it cannot be used to describe the depolarization process.

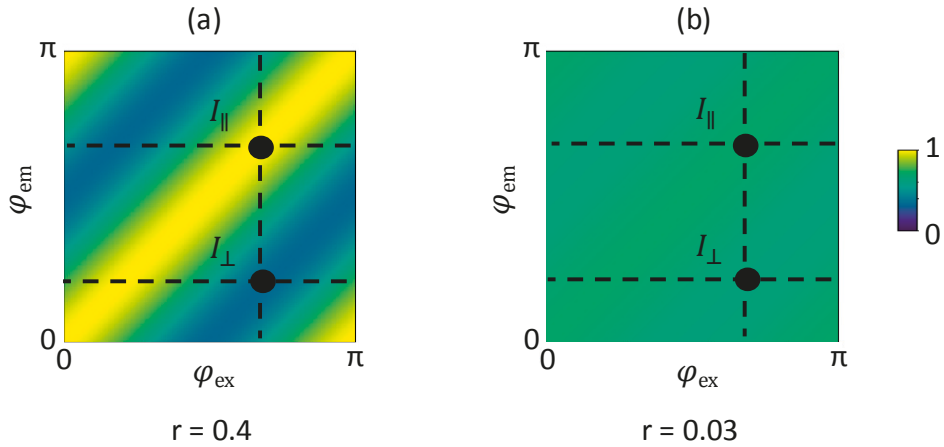

Figure 3.3. Calculate fluorescence anisotropy from polarization portrait for isotropic samples. (a) System has no depolarization processes (r = 0.4). (b) The system has efficient energy transfer processes resulting in r = 0.03.

3.3.2 Modulation depth correlation plot

The difference between excitation and emission polarization properties is a strong indication of energy transfer processes. It directly shows that the emitters are different from the initially excited absorbers. The modulation depth correlation plot and phase correlation plot directly show the relationship between the excitation and emission polarization properties of each object. These correlations can only be seen when M_{ex}, M_{em}, θ_{ex}, θ_{em} are obtained simultaneously for each object which is the case for the 2D POLIM technique.

Each data point in **Figure 3.4** represents an individual $MAPbI_3$ nanocrystal. The off-diagonal data points mean the object has different absorption and emission polarization properties (M and θ). Note that the studied objects on the phase correlation plot possess modulation depths higher than 0.07. If the modulation depth is close to zero, the phase is just an artificial number without any physical meaning. To make sure the meaning of the phase correlation plot, the data points in the phase correlation plot need to be selected in advance.

In the modulation depth correlation plot (**Figure 3.4a**), the emission becomes more polarized (less polarized) than the absorber if the data point close to the y-axis (x-axis). In the phase correlation plot (**Figure 3.4b**), the more off the diagonal, the larger the luminescence shift (LS) is. LS indicates that the object absorbs the maximum amount of light in one orientation, but the maximum emission intensity happens in another orientation.

Having M and θ difference is sufficient but not a necessary indication of energy transfer. Depending on the internal structure of the sample, it is possible that there

is efficient ET, while, the M and θ are the same for excitation and emission. For example, two dipoles orient orthogonally, and they exchange energy completely. The excitation and emission curve will be the same ($M_{ex} = M_{em} = 0$). However, we can distinguish the systems with or without ET clearly from 2D portrait.

This is because M and θ are calculated by the integral over the 2D portrait. The integral results in the loss of information. In contrast, 2D portrait contains more about the correlation between excitation and emission. The following section will show a unique parameter - energy funneling efficiency, which can only be extracted from the two-dimensional polarization portrait.

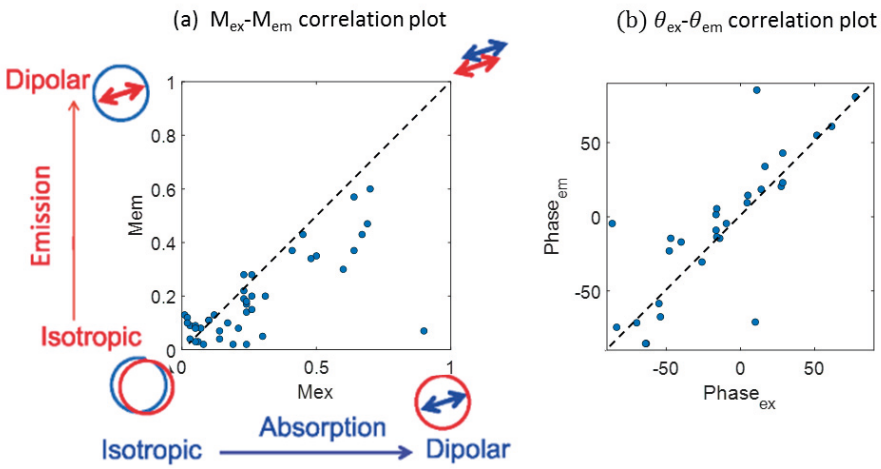

Figure 3.4. Examples of (a) a modulation depth correlation plot and (b) a phase correlation plot. The data points are measured from individual $MAPbI_3$ nanocrystals.

3.3.3 Energy funneling efficiency

Energy funneling is an essential concept in light-harvesting devices and in the single-molecule spectroscopy community.[56–58] Energy funnel efficiency is the ability of a system to transport the excitation energy towards a particular site. In this section, we introduce how to extract energy funneling efficiency from a 2D portrait. The following content refers to the previous work done by Rafael et al.[59]

For a single system consisted of N chromophores, a general description of the fluorescence intensity $I(\varphi_{ex}, \varphi_{em})$ measured by 2D POLIM is:

$$I(\varphi_{ex}, \varphi_{em}) = \sum_{i=1}^{N} \cos^2\left(\varphi_{ex} - \theta_i^0\right) \cos^2\left(\varphi_{em} - \theta_i^0\right) \qquad (3.11)$$

where N is the number of chromophores in the system, θ_i is the orientation of the chromophore *i*.

If there is ET process between the chromophores, then the excitation energy generated at chromophore *i* could be emitted by another chromophore *k*. To take this into account, we write:

$$I(\varphi_{ex}, \varphi_{em}) = \sum_{i=1}^{N} \cos^2\left(\varphi_{ex} - \theta_i^0\right) \sum_{k=1}^{N} T_{ik} \cos^2\left(\varphi_{em} - \theta_k^0\right) \tag{3.12}$$

where T_{ik} is a two-dimensional matrix describing the energy redistribution between chromophores:

$$T = \begin{bmatrix} t_{1\to1} & t_{1\to2} & \cdots & t_{1\to N} \\ t_{2\to1} & t_{2\to2} & & t_{2\to N} \\ \vdots & & \ddots & \vdots \\ t_{N\to1} & t_{N\to2} & \cdots & t_{N\to N} \end{bmatrix} \tag{3.13}$$

The elements t_{ik} tell how much energy transfers from chromophore i to chromophore k. Each column represents one chromophore. The sum of elements in column k represents the total energy emitted from chromophore k.

The 2D function $I(\varphi_{ex}, \varphi_{em})$ can be fitted with a linear combination of two limiting cases: NoET part – emission only from the chromophore i, and ET part- emission from the other chromophores due to energy transfer:

$$I(\varphi_{ex}, \varphi_{em}) = NoET + ET \tag{3.14}$$

$$NoET = \sum_{i=1}^{N} t_{ik(i=k)} \cos^2(\varphi_{ex} - \theta_i^0) \cos^2(\varphi_{em} - \theta_i^0) \tag{3.15}$$

$$ET = \sum_{i=1}^{N} \cos^2\left(\varphi_{ex} - \theta_i^0\right) \sum_{k=1}^{N} t_{ik(i\neq k)} \cos^2\left(\varphi_{em} - \theta_k^0\right) \tag{3.16}$$

Let us define for each chromophore *i* the parameter ε_i as:

$$\varepsilon_i = \sum_{k=1}^{N} t_{ik(i\neq k)} \tag{3.17}$$

This parameter shows the fraction of energy initially present at chromophore i which is transferred to other chromophores.

After some re-arrangement, the above equations can be written as:

$$NoET = \sum_{i=1}^{N} (1 - \varepsilon_i) \cos^2\left(\varphi_{ex} - \theta_i^0\right) \cos^2\left(\varphi_{em} - \theta_i^0\right) \tag{3.18}$$

$$ET = \sum_{i=1}^{N} \varepsilon_i \cos^2\left(\varphi_{ex} - \theta_i^0\right) \frac{1}{2}[1 + Mf_i \cos(2[\varphi_{em} - \theta f_i])] \qquad (3.19)$$

where the polarization properties of the EET emitter assigned to chromophore *i* are described by the modulation depth Mf_i and orientation θf_i.

The above equation shows why it is difficult to analyze the EET process in multi-chromophoric systems. This is because a system of N chromophores contains N funnels possessing different modulation depth Mf_i, phase θf_i and energy transfer efficiency ε_i. Without prior knowledge of the systems' internal organization, it is impossible to extract all unknown parameters from experimental data.

The above equation for the ET part can be simplified by single funnel approximation (SFA). In this approximation, we assume that there is only one ET-emitter (the same for all chromophores) and the ET efficiency ε is the same for all chromophores. In the framework of SFA, the above equations take the following form:

$$NoET = (1 - \varepsilon) \sum_{i=1}^{N} \cos^2\left(\varphi_{ex} - \theta_i^0\right) \cos^2\left(\varphi_{em} - \theta_i^0\right) \qquad (3.20)$$

$$ET = \varepsilon \frac{1}{2}[1 + Mf \cos(2[\varphi_{em} - \theta f])] \sum_{i=1}^{N} \cos^2\left(\varphi_{ex} - \theta_i^0\right) \qquad (3.21)$$

The coefficient ε, so-called the energy funneling efficiency, ranges from zero when there is no EET (perfect photoselection), to one, for the perfect EET funneling case (no photoselection). It works as a scaling factor to characterize the light-collecting efficiency over the whole system to an EET-emitter (a funnel). ε is not affected by anisotropy of absorption (presence of linear dichroism) contrary to fluorescence anisotropy.

The EET emitter can be a single dipole emitter, a pool of chromophores or even the whole system itself. The polarization properties of the EET emitter, Mf modulation depth and emission phase θf can be extracted from the ET portrait.

Figure 3.5 visualizes the mathematics described above. For perfect energy funneling (the 2D portrait of the ET part, **Figure 3.5**, second column), the emission polarization properties are characterized by Mf and θf and they are independent of the excitation angle. This is the signature of energy finneling. However, the emission intensity of the ET emitter can depend on the excitation angle because the overall energy absorbed by the system can depend on the excitation polarization angles. The NoET portrait (**Figure 3.5**, third column) shows the signature of photoselection – the intensity is symmetrical against the diagonal. It means that the maximum emission always happens at the same orientation of the analyzer as the orientation of the excitation polarization.

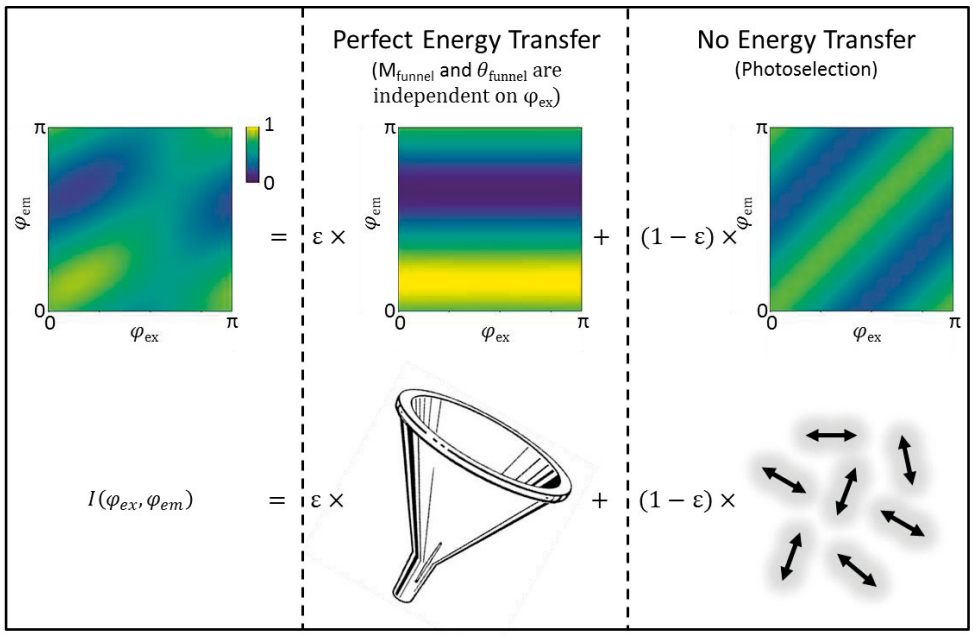

Figure 3.5. Decomposition of the polarization portrait (first column) into two separate portraits, one (the second column) corresponds to perfect energy funneling and the other (the third column) corresponds to no energy transfer.

The NoET part can be further expressed using the so-called symmetrical three-dipole model:

$$NoET = \frac{(1-\varepsilon)}{2+\Gamma}[\cos^2(\varphi_{ex} - [\theta_{ex} - \alpha])\cos^2(\varphi_{em} - [\theta_{ex} - \alpha] + \Gamma\cos^2(\varphi_{ex} - \theta_{ex})\cos^2(\varphi_{em} - \theta_{ex}) + \cos^2(\varphi_{ex} - [\theta_{ex} + \alpha])\cos^2(\varphi_{em} - [\theta_{ex} + \alpha])] \quad (3.22)$$

$$ET = \varepsilon\frac{1}{4}[1 + M_{ex}\cos(2[\varphi_{ex} - \theta_{ex}])][1 + Mf\cos(2[\varphi_{em} - \theta f])] \quad (3.23)$$

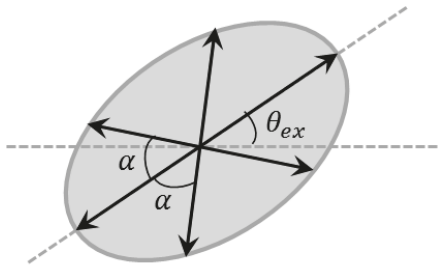

Figure 3.6. Three-dipole model.

The main dipole orients along the main axis of absorption of the system, thus this orientation is equal to θ_{ex}. Both side dipoles have the same absorption cross-section and are symmetrically oriented at an angle α respective to the main dipole. The ratio between the excitation cross-section of the main dipole and side dipoles is Γ. We need this formal presentation of the system to make it possible to fit experimentally measured 2D portraits.

Chapter 4 Results and discussions

4.1. Photo-oxidation reveals H-aggregates hidden in spin-cast conjugated polymer films – Paper I

Nowadays, conjugated polymers (CPs) are widely used in organic field-effect transistors (OFET),[60] organic light-emitting diodes (OLEDs),[61] photovoltaic cells (OPV),[62] and electrochemical transistors for bioelectronics and sensors.[63,64,65] Conjugated polymer chains can adopt different conformations which is important for the optical and electronic properties.

Single-molecule spectroscopy studies directly show highly oriented chain conformation possessing high polarization in absorption and emission,[66,67] but ensemble averaging in films eliminates the polarization anisotropy. However, depending on the chemical structure of conjugated polymers and substrate's surface energy, some polymers can form well-ordered micron-sized domains that are observable by optical microscopes. Preferential orientation on scales of millimeters and larger can be induced for CPs using external stimulus, including deposition on a liquid substrate,[68] mechanical rubbing,[69] epitaxial growth and unidirectional deposition techniques,[70] in-situ photo-polymerization on nematic liquid crystals[71] and other methods.

Exciton coupling can happen for the quasi-parallel and closely packed dense chains. It leads to the delocalization of the excitation over two or more segments in J-type (head to tail arrangement) or H-type (parallel arrangement) aggregates, resulting in a drastic change in the absorption and luminescence spectra. [20,21] (As discussed in Chapter 1, 1.2.2). Both oriented domains (H/J-aggregates) and amorphous phase could exist simultaneously in an actual spin-cast film.

This paper reports spontaneously formed highly oriented sub-micron domains in the spin-casting CP PBDT-TPD film observed by two-dimensional polarization imaging (2D-POLIM). A series of 2D POLIM contrast images of the same region of the film is obtained before and after photodegradation, as shown in **Figure 4.1** left column and right column, respectively. The emission modulation depth inhomogeneously increased during photodegradation which results in a clear microscale pattern. The film structure is not changed proved by atomic force microscopy (AFM) images. PL spectra of the fresh film and degraded film are very different. The intensity decreases 6.7 times, and the spectrum has a redshift from

664 nm to 704 nm. The 0-0 absorption transition relative to 0-1 transition is suppressed upon photodegradation.

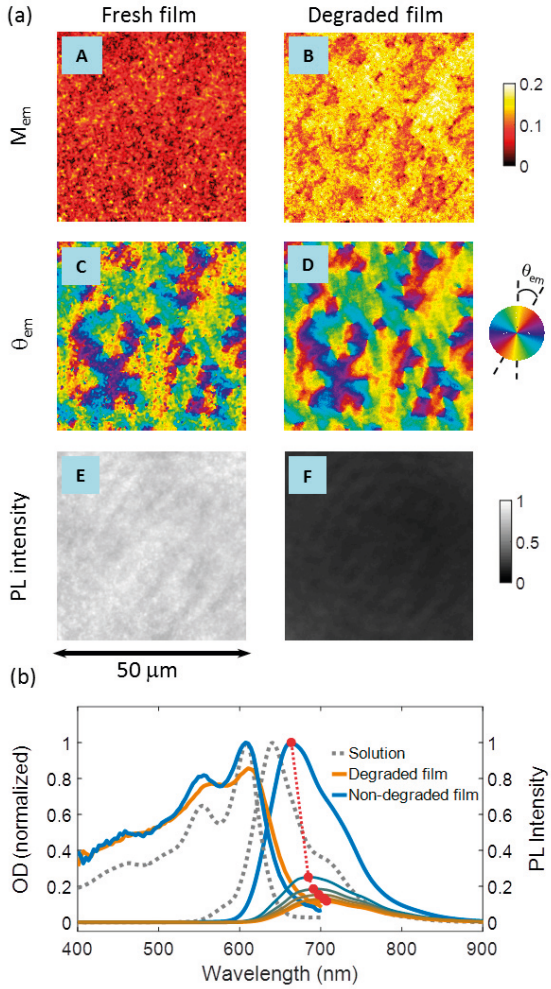

Figure 4.1 (a) Exemplary 2D POLIM images of the same position on the fresh (left column) and degraded (right column) PBDT-TPD film prepared on the glass substrate, spatial resolution is about 1 µm. The images in 2D POLIM contrasts are emission modulation depth M_{em} (A,B), modulation phase of emission θ_{em} (C,D), and fluorescence intensity (E,F). The size of the six images is 50 µm × 50 µm. (b) The PL and absorption spectra of isolated chains in dilute chloroform solution (grey dashed line) in comparison to those of the spin-cast film on a glass substrate (solid thick lines, blue-nondegraded film, orange-after 10 min of degradation). The absorption and PL spectra of the solution are normalized. PL spectra of the film were recorded every 2 min during photodegradation. These spectra are plotted in units of the maximum PL intensity of the fresh film. The red dashed line shows the redshift of the PL spectral maximum. Absorption spectra of the film before and after degradation are plotted in units of the maximum optical density of the fresh film.

The homogeneous film morphology indicates that the M_{em} and phase image pattern does not come from the defects of the film structure. These patterns should be micron-size-oriented domains hidden in the fresh film but become more visible in

the degraded film. Increasing of M_{em} indicates that the contribution of the PL of more oriented domains to the total PL intensity increases upon degradation.

We propose that the polymer film be a mixture of Phase 1 – less oriented and less photostable, and Phase 2 – more oriented and more photostable. M_{em} can be written as:

$$M_{em} = \beta_1 M_1 + \beta_2 M_2 \tag{4.1}$$

where M_1 and M_2 are the modulation depth of Phase 1 and Phase 2, and β_1 and β_2 are the contributions of each phase to the total PL ($\beta_1 + \beta_2 = 1$). Combining this equation with our experiment results (M_{em} = 0.07 and 0.14 before and after degradation, respectively), we can estimate the modulation depth of Phase 1 and Phase 2 is about 0.05 and 0.14 for the film on the glass. And β_1 decreases from 0.71 to 0, β_2 increases from 0.29 to 1 upon photodegradation.

A similar experiment we also have done for the film spin-casted on a silicon substrate. Due to the lower surface energy, polymers are more oriented on silicon substrates where M_1 is about 0.17 – 0.3, and $M_2 \approx 0.4$.

In the following discussion, we assign Phase 1 as amorphous phase, and Phase 2 as H-aggregates due to the obvious suppression of 0-0 transition in the absorption spectra. Furthermore, photodegradation destroys and converts the emitting sites to luminescence quenchers, leading to suppressing the overall PL intensity. In Phase 1 (less oriented or say amorphous phase), the overlap between its absorption and PL spectra is larger than H-aggregates in Phase 2. Thus, the Förster resonance energy transfer (FRET) efficiency is higher in Phase 1 than Phase 2. Due to the efficient FRET, one quencher in Phase 1 can quench a large film volume and cause significant suppression of the emission. However, the quenchers forming in Phase 2 do not substantially influence the PL of other aggregates due to insufficient energy transfer. That is why the PL intensity of Phase 1 decreases more than Phase 2 upon photodegradation.

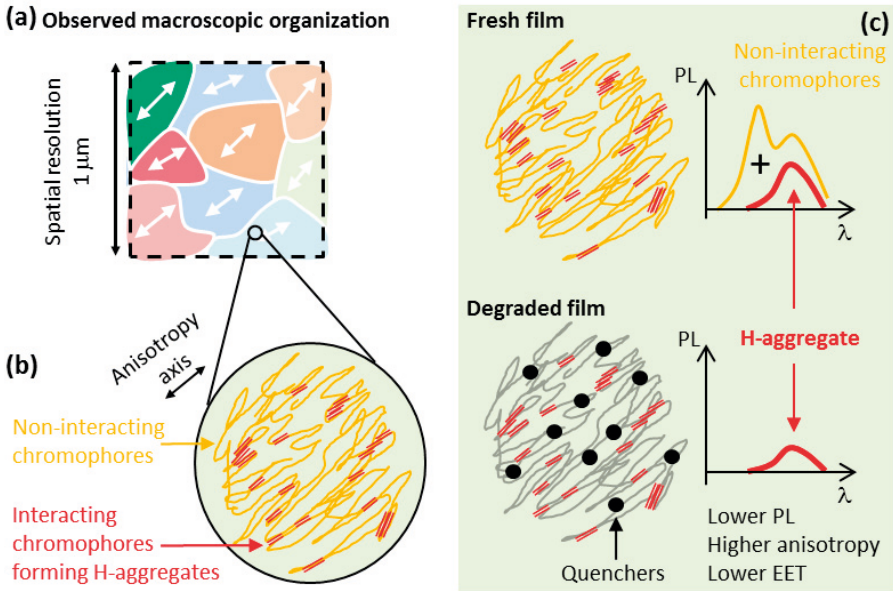

Figure 4.2 (a) Proposed local organization of the observed films with our spatial resolution. (b) Proposed microscopic organization of one domain. Yellow long lines show polymer chains that do not have strong interaction between chain segments but still follow the principal global orientation axis (Phase 1). The double red lines show parallel segments having substantial excitonic interaction forming H-aggregates (Phase 2). The emission of H-aggregate is red-shifted. (c) PL spectra of fresh and photodegraded films. PL of the fresh film is the sum of the PL of individual segments (Phase 1) and the PL of H-aggregates (Phase 2). The degraded film emits red-shifted PL (emission of H-aggregates) because the PL of individual segments is quenched due to efficient FRET to the photogenerated quenchers (black dots) formed in the nonaggregated phase.

In this paper, we demonstrated that photo-oxidation could be used to visualize hidden morphological structures. It turns out that depending on the local peculiarities of electronic and vibrational transitions and energy transfer, the resistance of the CPs luminescence to photodegradation-induced quenching can be very different. The diversity of structural organization is expected to affect the fundamental photoelectronic process relevant to understanding and improving polymer-based organic photovoltaic devices.

4.2 Strong photoluminescence polarization of $MAPbBr_3$ nano-structures – Paper II

Metal halide perovskites (MHPs) is a popular choice among the contemporary materials with great promises in optoelectronics as rendering from their efficacy and purity of photon emission.[72,73] Polarized light emission from nanocrystals (NCs) of MHPs will be beneficial for optoelectronic applications (e.g., LCD). Thus, polarized

light emission from MHPs and their control started to be an important topic in the field.

Polarized photoluminescence (PL) has been reported on metal halide perovskite (MHP) nano and microcrystals.[4,29,74–78] Generally, polarization in MHP nano and microcrystal may originate from the dielectric contrast,[27,79,80] exciton fine structure splitting in quantum confined nanostructures,[25,26,81] distortion of the crystal lattice and anisotropic orientation of TDMs,[29,30] or combination of more than one of these factors. However, in many cases, the polarization degree was not quantitatively compared with theory.

Several years ago, the synthesis of $MAPbBr_3$ NCs in a stretched polymer matrix *in-situ* was demonstrated.[4,73,82,83] This method leads to the formation of highly stable NCs embedded in the polymer film and exhibit strongly polarized excitation. The formation of NCs in a polymer matrix is a complicated process. As a result, the geometry of the NCs is very irregular compared to the widely studied nanocubes[78,30,76] or nanowires.[83–86]. Thus, it is important to know the structure of the individual object presented in the polymer matrix. This calls for the combination of fluorescence and electron microscopy.

In this contribution, we investigated polarization properties of the *in situ* fabricated $MAPbBr_3$ nano-structures in the stretched Polyvinylidene fluoride (PVDF) films employing spatially correlated high-resolution scanning electron microscopy (SEM) and two-dimensional polarization imaging (2D POLIM). We show that the topology and polarization properties of the particles inside the film vary considerably with the mass fraction of the perovskite. We find that an ordinary dielectric contrast model cannot explain all the polarization properties, and some weak elongated aggregates possess much stronger polarization than expected.

We studied two limiting concentrations (9%, high-C and 0.5%, low-C) of $MAPbBr_3$ perovskite in the polymer film. **Figure 4.3** shows SEM images of the representative films. The high-C film contains a large number of 'rice-like' nano-structures possessing an elongated shape oriented along the stretching direction (**Figure 4.3**, panel I, a). According to the previous study,[4] rice-like aggregates consist of several closely situated small nanocrystals of 5 – 10 nm in diameter aligned along the stretching direction. Interestingly, in the low-C film, we see only sub-micrometer stone-like aggregates, and no rice-like aggregates can be seen in the background (**Figure 4.3**, panel II, a).

To obtain the polarization properties of the different nano-structures, we use pixel analysis and single object analysis to calculate the polarization parameters (M and θ) of rice-like aggregates (in the high-C film) and individual stone-like aggregates (in the low-C film), respectively. For the high-C film, the M_{ex} (average $M_{ex} = 0.25$) and M_{em} (average $M_{em} = 0.36$) do not vary significantly across the low-C film (**Figure 4.3**, Panel I, cd). The excitation and emission phases coincide with the film stretching direction (shown by the arrows in **Figure 4.3**). In the low-C film, stone-

like aggregates can have quite different polarization properties, which can be seen from the wide distributed data point in the modulation depth correlation plot (**Figure 4.3**, Panel II, c). There are two sub-populations that are marked as Group 1 and Group 2. Surprisingly, some of the stone-like aggregates have extremely high M_{ex} = 0.88 and 0.78 (**Figure 4.3**, Panel II, a).

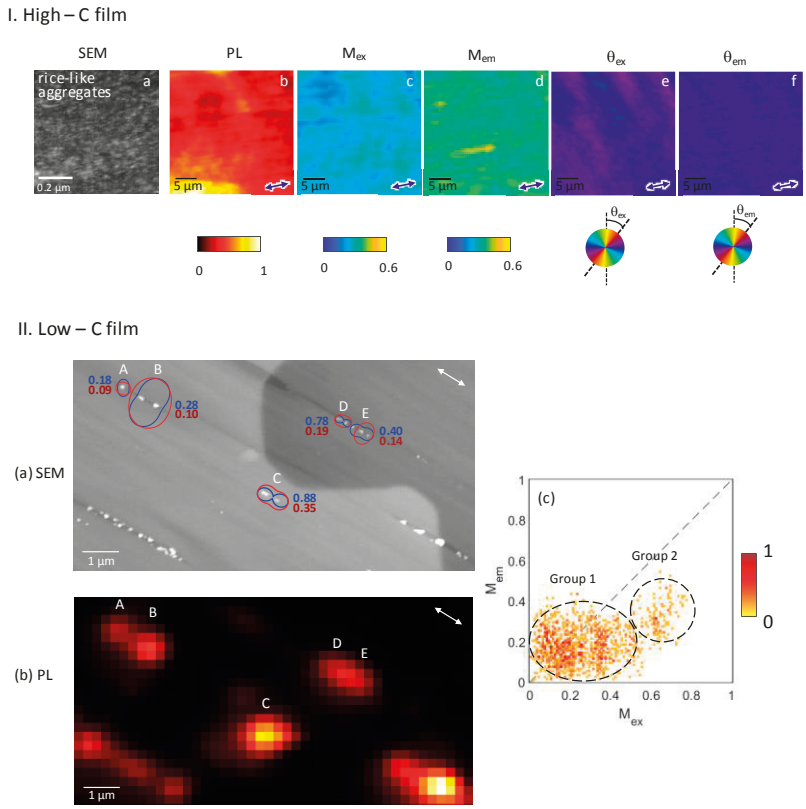

Figure 4.3. Polarization properties and SEM images of (I) high-C and (II) low-C films. In Panel I, (a-g) are the high-resolution SEM image, fluorescence intensity, excitation modulation depth (M_{ex}), emission modulation depth (M_{em}), excitation phase (θ_{ex}), emission phase (θ_{em}) images of the high-C film. In Panel II, (a) SEM image of stone-like aggregates overlaid with their polar plots showing the polarization property of excitation (blue) and emission (red). (b) is the PL images of the same position shown in the SEM image (a). (c) 2D density distribution of excitation and emission modulation depth for low-C films. Two subpopulations are shown (group 1 and group 2, marked in dashed circles) in the low-C film.

The dielectric screening effect can result in polarized absorption and emission of elongated objects. When a dielectric material is placed in a static electric field, an internal electric field E_i is generated due to the charge accumulation on the object's inner surface. This internal electric field attenuates the applied field inside the nano-structures, producing local electric field $E = E_0 - E_i$. This is the so-called dielectric screening effect. Due to the elongation of the object, $E_{\parallel} > E_{\perp}$.

Considering dielectric contrast, we calculate polarization properties numerically by solving Maxwell equations for the desired structure and compare them with the experimental data. We build four closely located spheres (diameter is 6 nm) as a model of rice-like aggregates (**Figure 4.4**, Panel I) and calculate M_{ex} and M_{em} for different arrangements of four spheres. At first glance, all these results capture pretty well the experimentally observed polarization properties of the high-C film (**Figure 4.3**, Panel I, cd). Additionally, we learned that i) both M_{ex} and M_{em} increase with increasing the overlapping between the spheres (**Figure 4.4**, Panel I, b), ii) the aggregate can have higher M_{em} if the emission site is closer to the object's center (**Figure 4.4**, Panel I, c). The second observation might explain why $M_{em}>M_{ex}$ from our experimental results (**Figure 4.3**, Panel I, cd).

We chose the object C possessing M_{ex} = 0.88 and M_{em} = 0.35 and calculate its polarization properties based on its geometry. Calculations gave M_{ex} = 0.31 and M_{em} = 0.33. The experimental M_{ex} is more than two times larger than expected from the theory. We varied several features of the object geometry, such as distance between individual particles in the aggregates, presence of the resonance effects by adjusting the size of the ellipsoid, and placing the aggregate into a cavity filled with air. However, we were not able to achieve the experimentally observed averaged M_{ex} (experiment) = 0.7. Thus, we conclude that the dielectric screening effect semi-quantitatively explains the polarization properties of stone-like aggregates in Group 1, but not in Group 2. So far, we have only one idea with the potential to rationalize the high polarization degree. It has been observed in several studies on $MAPbBr_3$ materials that the PL intensity grows nonlinearly with the excitation power.[87–89] This non-linear dependence of PL intensity on the excitation power can be partially responsible for the observed polarization higher than 0.6.

I. Rice-like aggregates in the high – C film

(a) Four spheres without overlap
M_{ex}: 0.24
M_{em}: 0.227

(b) Four spheres with overlap
M_{ex}: 0.3135
M_{em}: 0.322

(c) Emission from center and peripheral spheres
M_{em}(peripheral): 0.15
M_{em}(center): 0.27

(d) An array of rice-like aggregates
M_{ex}: 0.325
M_{em}: 0.312

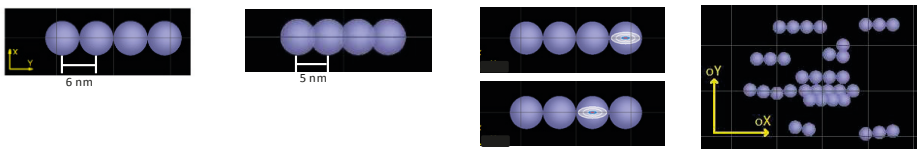

II. Stone-like aggregates in the low – C film

(a) Geometry of the object C

(b) Simulation and experiment results of the object C

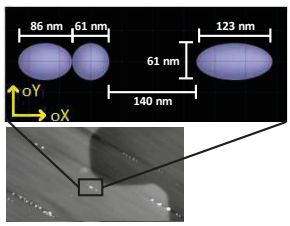

	Simulation (Geometry in (a))	Experiment (Geometry in (a))
M_{ex}	0.27	0.88
M_{em}	0.33	0.35
$Phase_{ex}$	elongation direction	68.5°
$Phase_{em}$	elongation directon	59.5°

Figure 4.4. In Panel I, a list of M_{ex} and M_{em} for rice-like aggregates consisting (a) four spheres without overlap and (b) four spheres with overlap. (c) M_{em} is higher when the emitting site is close to the center of the object. (d) M_{ex} and M_{em} of an array of rice-like aggregates. Each sphere represents one nanocrystal. The diameter of one sphere is 6 nm. In Panel II, (a) the geometry of the object C. (b) a summary of simulation and experiment results of the Object C.

To summarize, we studied the polarization properties of three different types of $MAPbBr_3$ nano-structures fabricated *in situ* in stretched PVDF films. They are rice-like aggregates, stone-like aggregates in Group 1, and stone-like aggregates in Group 2. We find the dielectric screening effect can semi-quantitatively explain the polarization of rice-like aggregates and stone-like aggregates in Group 1, but cannot explain the high M_{ex} from Group 2. Resonance effects when the size of the objects becomes comparable with the wavelength also cannot allow reaching the required level of M_{ex}. Non-linear dependence of PL intensity on the excitation power can be part of the reason. More theoretical and experimental research is needed to explain the observed phenomenon.

4.3 Characterization and improvement of single funnel approximation (SFA) – Paper III and Paper IV

Förster resonance energy transfer (FRET) is a nonradiative energy transfer between a donor (D) in the excited state and an accepter (A) in the ground state. When the donor and the accepter have distinguishable absorption and luminescence spectra, it is so-called hetero-FRET. Otherwise, homo-FRET can take place between two like

fluorophores (e.g., green fluorescent protein). Generally, fluorescence anisotropy (FA) is a powerful tool to study the homo-FRET efficiency of isotropic samples.[55,90–93]

Our group developed an advanced technique 2D POLIM, and the SFA model (as described in Chapters 2 and 3) quantitively assesses the energy transfer efficiency. This method has been successfully applied to various systems, such as single molecules,[21–23] blend CPs film,[96,53] natural light-harvesting system[93,94] and protein aggregation in biological cells.[97] In the following work, we do a series of computer experiments to test our SFA model on a known artificially generated system. This work allows us to learn the applicability of the SFA model and further improve it. The important results and discoveries are listed below:

1. In the absence of excitation energy transfer (EET), the curves (black curves, **Figure 3a-d**) on the diagonal of the 2D portrait has form: $I(\varphi_{ex} = \varphi_{em}) = \sum_{i=1}^{N} \cos^4(\varphi_{ex} - \theta_i^0)$. Theoretically, by using this equation to fit the diagonal of any portrait without EET, one can obtain the number and the orientation of chromophores. However, it will not work for an isotropic sample (**Figure 3c**). The above information cannot be seen from one-dimensional polarization measurements.

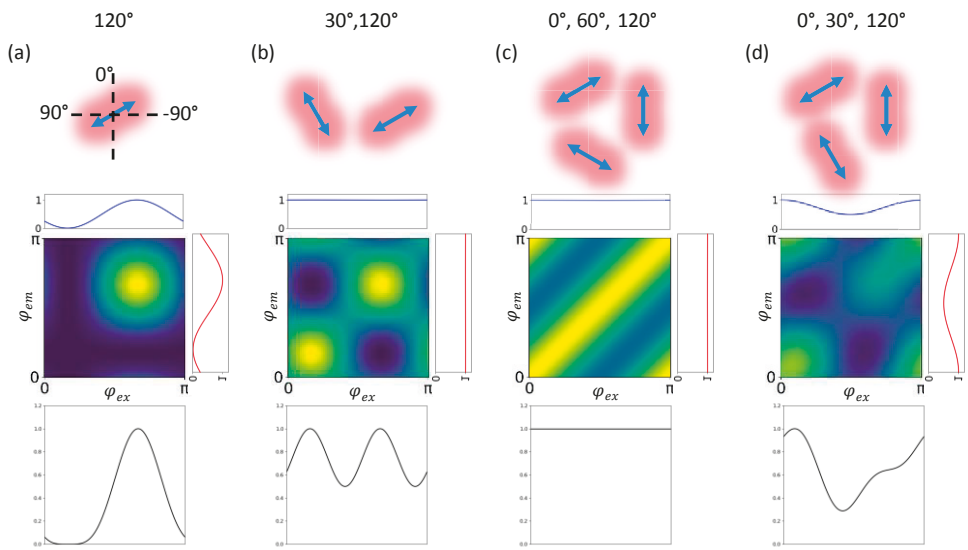

Figure 4.5. Examples of 2D portrait without ET. Excitation (blue curve on the top) and emission (red curve on the left) polarization property can be obtained by the integral over the y and x axis of 2D portrait, respectively. The black curves are the intensity on the diagonal of 2D portraits. (a) One chromophore orients at 120°. (b) Two chromophores orient at 30° and 120°, respectively. (c) Three chromophores orient at 0°, 60° and 120°, forming a system possessing isotropic absorption. (d) Three chromophores orient at 0°, 30° and 120°, respectively.

2. Multi-funnel system means several funnels exist in one system, and chromophores transfer different amounts of energy (ε_i) to the funnels. The SFA

funnel can be applied to multi-funnel systems if they meet the following requirements:

i) The multi-funnel system can be split into several sub-systems connected to each funnel. In each sub-system, only one funnel exists, and all the chromophores transfer the same amount of energy to it.

ii) The absorption polarization (defined by excitation modulation depth and excitation phase) of all the sub-systems is the same.

3. Based on the previous experience,[98] an asymmetric three-dipole model is designed to fit NoET portraits to get the orientation of the system. In comparison with the previous symmetric three-dipole model, the asymmetric model can be better used for the system where chromophores orient asymmetrically along the main axis of absorption.

The residues of the symmetric model are relatively high, especially when there is no energy transfer process in the system. More interestingly, the residues decrease with increasing energy funneling efficiency. This trend directly illustrates that energy transfer results in the loss of excitation information, or other words, loss of polarization memories.

Contrary to symmetric model, the residues keep low no matter there is efficient energy transfer or not, which means the asymmetric model works very well for the system. Note that the asymmetric model is more susceptible to the initial value. To apply the asymmetric three-dipole model to an actual situation, one needs to input more initial values or increase the iteration step until the fitting find the stable minimum value.

4. In this section, we do several computational tests on different arrangements of absorbers and emitters to address the following topics:

i) The relation between fluorescence anisotropy r and energy funnelling efficiency ε for randomly oriented molecules is $r = 2 \times \frac{1-\varepsilon}{5+\varepsilon}$. The higher the energy funneling efficiency, the lower the r will be.

ii) Fundamental fluorescence anisotropy r in 2D. As shown in **Figure 4.6b**, molecules randomly orient on a 2D plane, and the angle between the absorption and emission TDM is β. The dependence of r and β is $r(2D) = \frac{cos(2\beta)}{3-0.5\,cos(2\beta)}$. The relation between ε and β is $\varepsilon = 1 - \cos(2\beta)$. (**Figure 4.6c**)

iii) Energy funneling efficiency ε can be larger than one (negative fluorescence anisotropy) when β goes beyond the magic angle (**Figure 4.6c**). The magic angle is 45° in the case of 2D plane. Such negative fluorescence anisotropy has been

observed in many systems,[99–102] such as a three-dimensional π-conjugation molecular nanotube, a dimer of yellow fluorescent protein (YFP), phosphole oxide-based dyes in nematic liquid crystals, and J-aggregates. Surprisingly, our SFA model can also be applied in such complicated systems and expected to get ε > 1.

iv) The absorption polarization property can also affect energy funneling efficiency and has a relation $\varepsilon = 1 - M_{ex}$ (**Figure 4.6e**). If the absorption of the molecule is isotropic, ε is equal to 1. Otherwise, ε is equal to 0.

v) In **Figure 4.6 d and f**, we can say there is no energy transfer between molecules (inter-molecular ET), but the energy transfer within a molecule (intra-molecular ET) is very efficient. This means neither r nor ε can distinguish between inter- and intra-molecular ET.

vi) In paper IV, we present ε and r of the conjugated polymer pristine film studied in Paper I. The film possesses an inhomogeneous structure in terms of chain orientation. The variation in r is much greater than ε. It means ε is virtually insensitive to the degree of local alignment and gives images of energy transfer efficiency clearly from orientation artifacts. The related simulation results have also been calculated in previous work. [93]

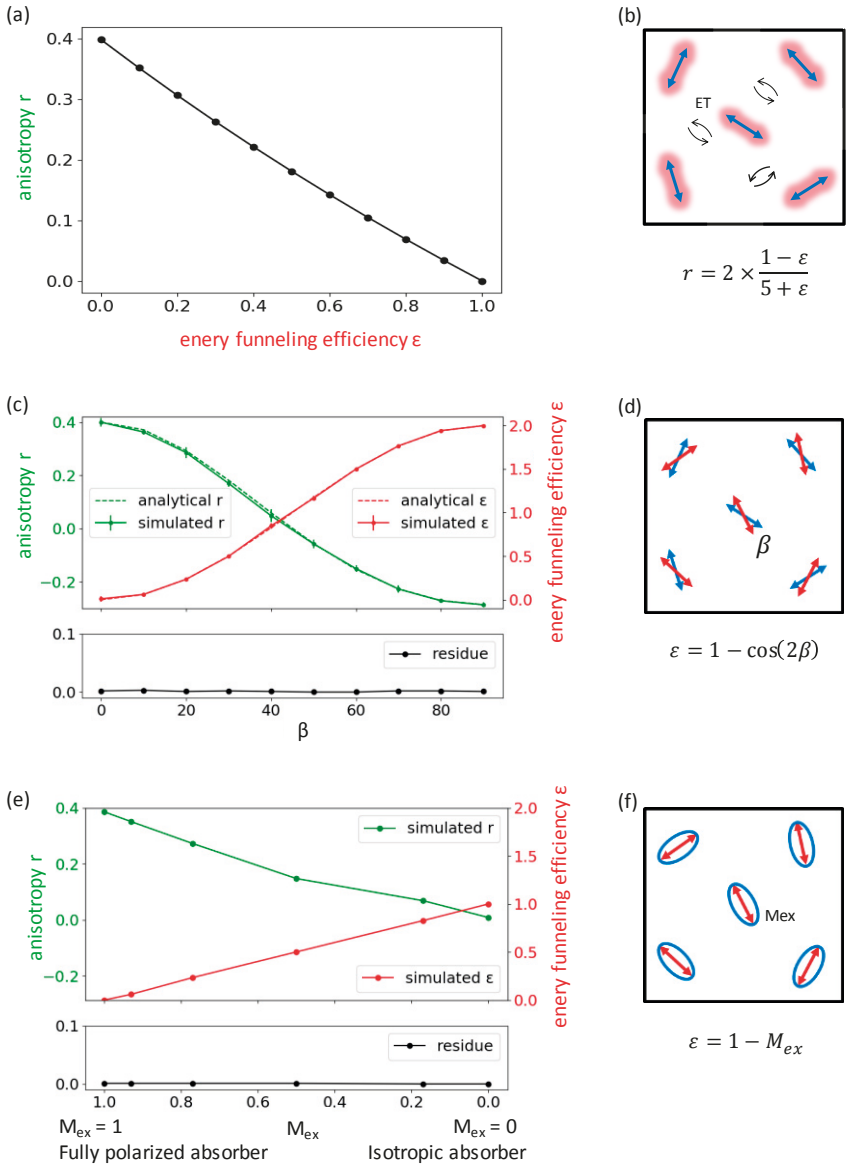

Figure 4.6. (a) present the relation between r and ε for 1000 random oriented molecules (same excitation and emission TDMs) on a 2D plane (b). (c) shows analytical solution (dashed line) and simulated results (solid line) of the β-r (green) and β-ε (red) dependence. (d) β it the difference between the orientation of absorption and emission TDMs. (e) shows the M_{ex}-r and M_{ex}-ε dependence. (f) M_{ex} is the absorption polarization. M_{ex} = 1 means fully polarized absorber. M_{ex} = 0 means isotropic absorber.

5. We found a crucial limitation of the SFA model. SFA model does not work for multi-systems possessing completely different absorption polarization and energy funneling efficiency, even if all the systems share the same funnel.

The above results help us to understand more about 2D portrait and the SFA model. The development of the model increases the model's utility. The knowledge will allow us to have an insightful understanding of the experimental data in the future.

Chapter 5 Conclusions and future work

5.1 Summary of the novelties in the thesis

Paper I, II and IV show that the two-dimensional polarization measurement, together with the SFA model, is a powerful tool to study the energy transfer process in semiconductor materials (e.g., conjugated polymers and perovskite nanocrystals) and in a biological sample (protein aggregation). 2D POLIM can be applied to bulk material (Paper I, IV) or single-molecule study (Paper II). In paper III, we did systematic learning of our single funnel approximation (SFA) model by doing a series of computer experiments. This work allows us to have more understanding of our model and energy funneling efficiency ε.

In paper I, we proposed that partial photodegradation of conjugated polymer (CP) films can help reveal the internal organization of the material. We also found that H-aggregation formation in the spin-cast film results in poor energy transfer efficiency between CP chains.

In paper II, we found that even irregular-shaped aggregates can have extreme excitation polarization. Such intense polarization cannot be explained by the well-known theory – dielectric screening effect. We propose that the non-linear dependence of PL intensity on the excitation power typical for semiconductors can be partially responsible for the observed high polarization.

In paper III, we found the extension of the SFA model (applied on multi-funnel systems) and developed an asymmetric three-dipole model. We broke the limit of ε (0, 1) and realized that ε goes beyond one when β is larger than the magic angle.

In paper IV, we showed that 2D POLIM and energy funneling efficiency ε can also be used as a low-cost fluorescence method to distinguish between non-aggregated and aggregated forms of α-synuclein.

5.2 Future work

5.2.1 Quantitative phase-contrast imaging

The ability of our home-built 2D POLIM setup can be further enhanced by adding quantitative phase-contrast imaging (2D POLIM+). The setup structure is shown in **Figure 5.1** right column. A polarizer is added to the fluorescence-based 2D POLIM, installed on the light path of a white light source used for light transmission imaging. A high-precision motorized stage should rotate this polarizer. So we can send linearly polarized white light of desired polarization orientation to the sample. Due to the local birefringence or/and anisotropic absorption, the polarization state of the transmitted light will be changed. This change will be quantitatively recorded by rotating the analyzer installed in front of the camera. Using bandpass filters, we can measure birefringence in the desired spectral range and distinguish it from a selective anisotropic absorption. The whole measurement can be automated using a home-built Labview software.

Combining the fluorescence-based polarization contrasts with the light transmission polarization contrasts will allow us to quantitatively characterized anisotropy of biological systems at two fundamentally different levels simultaneously: i) molecular structures labeled by the dyes at the nanoscale and ii) cellular structures label-free at the micro-scale.

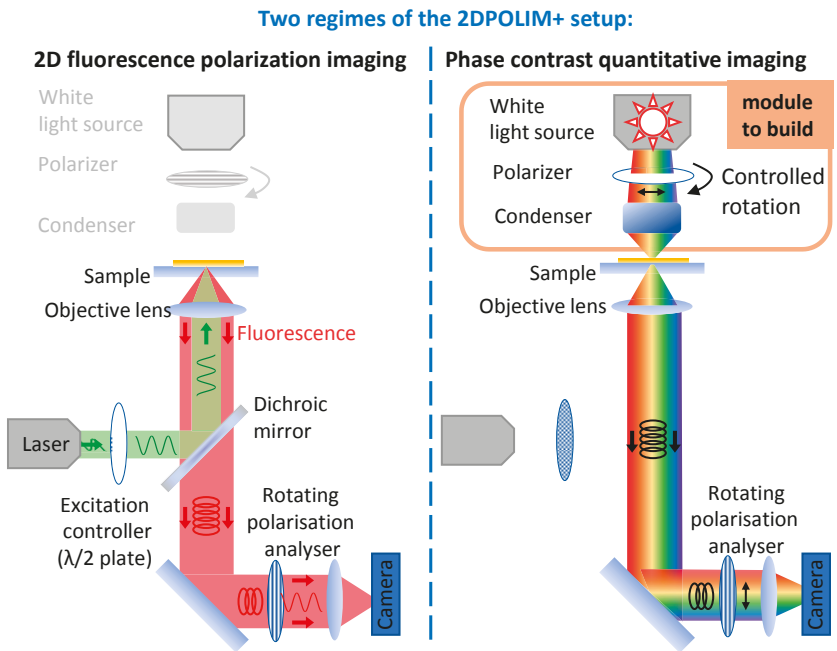

Figure 5.1 fluorescence-based 2D POLIM (left column) and enhanced phase contrast 2D POLIM+ (right column).

5.2.2 Time-resolved two-dimensional polarization imaging

Combining 2D POLIM and TCSPC, one can measure time-resolved polarization imaging. This is another exciting direction for the further development of 2D POLIM. The scheme of the setup is shown in **Figure 5.2**. A series of polarization portraits will be obtained on the scale of molecules lifetime, and this will allow us to observe the evolution of the excitation energy transfer (EET) process and the change of chain conformation during the lifetime. For this measurement, the samples need to be photo-stable, and the EET process is slower than the time resolution of the setup.

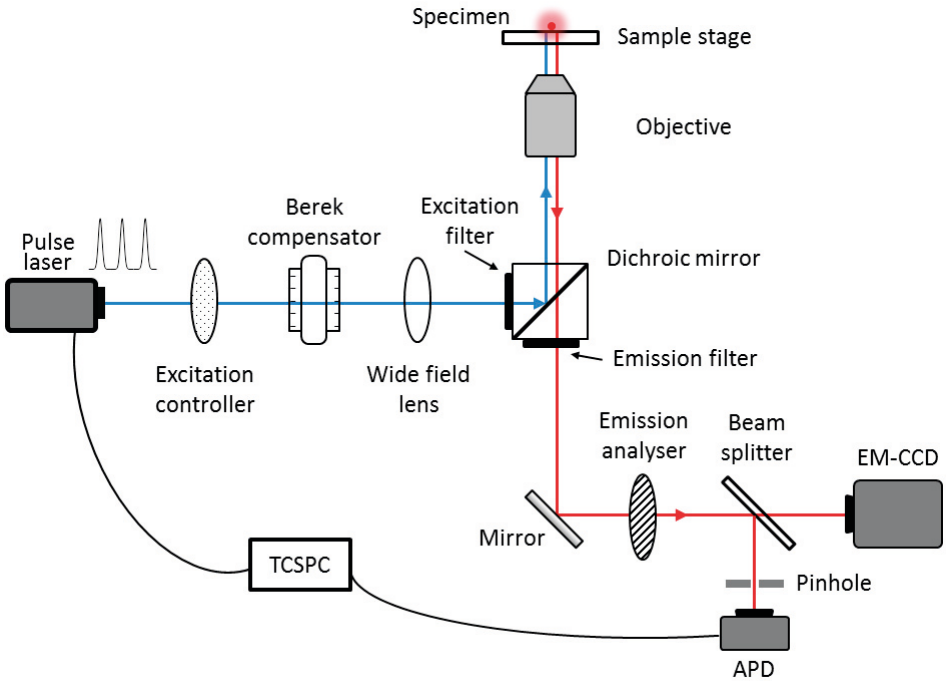

Figure 5.2 Scheme of time-resolved 2D POLIM setup.

Appendix

Calculate anisotropy for dipoles randomly oriented in 2D plane.

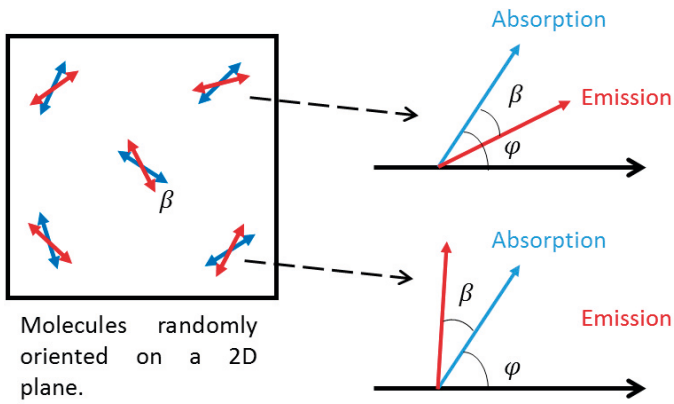

Figure A1. One dipole orients at angle φ. The angle between its absorption and emission transition dipole moments is β.

To measure the anisotropy of an isotropic sample, we use linearly polarized light to excite the sample and measure the fluorescence intensity parallel $I_{\parallel}$ and perpendicular $I_{\perp}$ to the direction of excitation electric field E. First, we consider the electric field interacts with one dipole oriented on angle φ, as shown in **Figure A1**. In order to keep the symmetry of the geometry same as in the real situation, we assume the emission transition dipole moment can be rotated either to the left (+β) or to the right (-β). So we have emission intensity:

$$I_{\parallel} = sin^2\varphi\, sin^2(\varphi - \beta) + sin^2\varphi\, sin^2(\varphi + \beta) \qquad (A.1)$$

$$I_{\perp} = sin^2\varphi\, sin^2(\varphi - \beta) + sin^2\varphi\, sin^2(\varphi + \beta) \qquad (A.2)$$

To calculate the anisotropy of an ensemble sample, we need to integrate the angle φ from 0 to 2π and calculate the average value, so we get:

$$< I_{\parallel} + I_{\perp} > = < 2sin^2\varphi >= 1 \qquad (A.3)$$

$$< I_{\parallel} - I_{\perp} > = < 2sin^2\varphi\, cos2\varphi\, cos2\beta >= \frac{1}{2} cos2\beta \qquad (A.4)$$

The polarization P can be calculated by:

$$P = \frac{< I_{\parallel} - I_{\perp} >}{< I_{\parallel} + I_{\perp} >} = \frac{1}{2} cos2\beta \qquad (A.5)$$

And anisotropy r = 2P/(3-P), so:

$$r = \frac{cos2\beta}{3 - 0.5cos2\beta} \qquad (A.6)$$

The above equations calculate the anisotropy of an ensemble sample on a 2D plane. The maximum value of r is 0.4 when the absorption and emission transition dipole moment are overlapped (β = 0°). r is equal to 0 if β = 45° (magic-angle in the case of 2D). And the minimum value of r = -2/7 when β = 90°.

References

(1) Yang, Y.; Kelley, K.; Sachet, E.; Campione, S.; Luk, T. S.; Maria, J. P.; Sinclair, M. B.; Brener, I. Femtosecond Optical Polarization Switching Using a Cadmium Oxide-Based Perfect Absorber. *Nat. Photonics* **2017**, *11* (6), 390–395.

(2) Wu, D.; Guo, J.; Du, J.; Xia, C.; Zeng, L.; Tian, Y.; Shi, Z.; Tian, Y.; Li, X. J.; Tsang, Y. H.; Jie, J. Highly Polarization-Sensitive, Broadband, Self-Powered Photodetector Based on Graphene/PdSe2/Germanium Heterojunction. *ACS Nano* **2019**, *13* (9), 9907–9917.

(3) Bharadwaj, P.; Deutsch, B.; Novotny, L. Optical Antennas. *Adv. Opt. Photonics* **2009**, *1* (3), 438.

(4) Lu, W. G.; Wu, X. G.; Huang, S.; Wang, L.; Zhou, Q.; Zou, B.; Zhong, H.; Wang, Y. Strong Polarized Photoluminescence from Stretched Perovskite-Nanocrystal-Embedded Polymer Composite Films. *Adv. Opt. Mater.* **2017**, *5* (23), 1–8.

(5) Hafi, N.; Grunwald, M.; Van Den Heuvel, L. S.; Aspelmeier, T.; Chen, J. H.; Zagrebelsky, M.; Schütte, O. M.; Steinem, C.; Korte, M.; Munk, A.; Walla, P. J. Fluorescence Nanoscopy by Polarization Modulation and Polarization Angle Narrowing. *Nat. Methods* **2014**, *11* (5), 579–584.

(6) Hecht, E. *Optics*; Addison-Wesley, 2002.

(7) Lakowicz, J. R. *Principles of Fluorescence Spectroscopy*; Springer-Verlag New York Inc., 2006.

(8) Kliger, D. S.; Lewis, J. W. *Polarized Light in Optics and Spectroscopy*; Academic press, 1990.

(9) Samori', B.; Thulstrup, E. W. *Polarized Spectroscopy of Ordered Systems*; Kluwer Academic, 1988.

(10) Krause, S.; Neumann, M.; Fröbe, M.; Magerle, R.; Von Borczyskowski, C. Monitoring Nanoscale Deformations in a Drawn Polymer Melt with Single-Molecule Fluorescence Polarization Microscopy. *ACS Nano* **2016**, *10* (2), 1908–1917.

(11) Liu, Y.; Wu, Z.; Liu, X.; Han, S.; Li, Y.; Yang, T.; Ma, Y.; Hong, M.; Luo, J.; Sun, Z. Intrinsic Strong Linear Dichroism of Multilayered 2D Hybrid Perovskite Crystals toward Highly Polarized-Sensitive Photodetection. *Adv. Opt. Mater.* **2019**, *7* (23), 2–7.

(12) Wu, J.; Cong, X.; Niu, S.; Liu, F.; Zhao, H.; Du, Z.; Ravichandran, J.; Tan, P. H.; Wang, H. Linear Dichroism Conversion in Quasi-1D Perovskite

Chalcogenide. *Adv. Mater.* **2019**, *31* (33).
(13) Wemyss, A. M.; Razmkhah, K.; Chmel, N. P.; Rodger, A. Fluorescence Detected Linear Dichroism of Small Molecules Oriented on Polyethylene Film. *Analyst* **2018**, *143* (23), 5805–5811.
(14) Clegg, R. M.; Sener, M.; Govindjee. From Förster Resonance Energy Transfer to Coherent Resonance Energy Transfer and Back. *Soc. Photo-Optical Instrum. Eng. Conf. Ser.* **2010**, 1–21.
(15) Köhler, A.; Bässler, H. *Electronic Processes in Organic Semiconductors: An Introduction*; John Wiley & Sons, 2015.
(16) Heeger, A. J. Semiconducting Polymers: The Third Generation. *Chem. Soc. Rev.* **2010**, *39* (7), 2354–2371.
(17) McNeill, C. R. Imaging the Domain Structure of Organic Semiconductor Films. *J. Polym. Sci., Part B Polym. Phys.* **2011**, *49* (13), 909–919.
(18) Kasha, M. Energy Transfer Mechanisms and the Molecular Exciton Model for Molecular Aggregates. *Radiat. Res.* **1963**, *20* (1), 55–70.
(19) Spano, F. C. Absorption in Regio-Regular Poly(3-Hexyl)Thiophene Thin Films: Fermi Resonances, Interband Coupling and Disorder. *Chem. Phys.* **2006**, *325* (1), 22–35.
(20) Spano, F. C. The Spectral Signatures of Frenkel Polarons in H- and J-Aggregates. *Acc. Chem. Res.* **2010**, *43* (3), 429–439.
(21) Hestand, N. J.; Spano, F. C. Expanded Theory of H- and J-Molecular Aggregates: The Effects of Vibronic Coupling and Intermolecular Charge Transfer. *Chem. Rev.* **2018**, *118* (15), 7069–7163.
(22) Yamagata, H.; Hestand, N. J.; Spano, F. C.; Köhler, A.; Scharsich, C.; Hoffmann, S. T.; Bässler, H. The Red-Phase of Poly[2-Methoxy-5-(2-Ethylhexyloxy)- 1,4-Phenylenevinylene] (MEH-PPV): A Disordered HJ-Aggregate. *J. Chem. Phys.* **2013**, *139* (11), 114903.
(23) Parson, W. W. *Modern Optical Spectroscopy*; Springer-Verlag Berlin Heidelberg, 2015.
(24) Kojima, A.; Teshima, K.; Shirai, Y.; Miyasaka, T. Organometal Halide Perovskites as Visible-Light Sensitizers for Photovoltaic Cells. *J. Am. Chem. Soc.* **2009**, *131* (17), 6050–6051.
(25) Sercel, P. C.; Vahala, K. J. Polarization Dependence of Optical Absorption and Emission in Quantum Wires. *Phys. Rev. B* **1991**, *44* (11), 5681–5691.
(26) Sercel, P. C.; Vahala, K. J. Analytical Technique for Determining the Polarization Dependence of Optical Matrix Elements in Quantum Wires with Band-Coupling Effects. *Appl. Phys. Lett.* **1990**, *57* (6), 545–547.
(27) Ruda, H. E.; Shik, A. Polarization-Sensitive Optical Phenomena in Semiconducting and Metallic Nanowires. *Phys. Rev. B* **2005**, *72* (11), 115308.
(28) Ruda, H. E.; Shik, A. Polarization-Sensitive Optical Phenomena in Thick Semiconducting Nanowires. *J. Appl. Phys.* **2006**, *100* (2).
(29) Täuber, D.; Dobrovolsky, A.; Camacho, R.; Scheblykin, I. G. Exploring the

Electronic Band Structure of Organometal Halide Perovskite via Photoluminescence Anisotropy of Individual Nanocrystals. *Nano Lett.* **2016**, *16* (8), 5087–5094.

(30) Jurow, M. J.; Lampe, T.; Penzo, E.; Kang, J.; Koc, M. A.; Zechel, T.; Nett, Z.; Brady, M.; Wang, L. W.; Alivisatos, A. P.; Cabrini, S.; Brütting, W.; Liu, Y. Tunable Anisotropic Photon Emission from Self-Organized $CsPbBr_3$ Perovskite Nanocrystals. *Nano Lett.* **2017**, *17* (7), 4534–4540.

(31) Jurow, M. J.; Morgenstern, T.; Eisler, C.; Kang, J.; Penzo, E.; Do, M.; Engelmayer, M.; Osowiecki, W. T.; Bekenstein, Y.; Tassone, C.; Wang, L. W.; Alivisatos, A. P.; Brütting, W.; Liu, Y. Manipulating the Transition Dipole Moment of CsPbBr 3 Perovskite Nanocrystals for Superior Optical Properties. *Nano Lett.* **2019**, *19* (4), 2489–2496.

(32) Landau, L. D.; Lifshitz, E. M. *Electrodynamics of Continuous Media*; 2015; Vol. 42.

(33) Hwang, I.; Scholes, G. D. Electronic Energy Transfer and Quantum-Coherence in π-Conjugated Polymers. *Chem. Mater.* **2011**, *23* (3), 610–620.

(34) Schwartz, B. J.; Nguyen, T. Q.; Wu, J.; Tolbert, S. H. Interchain and Intrachain Exciton Transport in Conjugated Polymers: Ultrafast Studies of Energy Migration in Aligned MEH-PPV/Mesoporous Silica Composites. *Synth. Met.* **2001**, *116* (1–3), 35–40.

(35) Schwartz, B. J. Conjugated Polymers as Molecular Materials : How Chain Conformation and Film Morphology Influence Energy Transfer and Interchain Interactions. *Annu. Rev. Phys. Chem.* **2003**, *54* (1), 141–172.

(36) Scheblykin, I. G.; Yartsev, A.; Pullerits, T.; Gulbinas, V.; Sundström, V. Excited State and Charge Photogeneration Dynamics in Conjugated Polymers. *J. Phys. Chem. B* **2007**, *111* (23), 6303–6321.

(37) Beljonne, D.; Pourtois, G.; Silva, C.; Hennebicq, E.; Herz, L. M.; Friend, R. H.; Scholes, G. D.; Setayesh, S.; Müllen, K.; Brédas, J. L. Interchain vs. Intrachain Energy Transfer in Acceptor-Capped Conjugated Polymers. *Proc. Natl. Acad. Sci. U. S. A.* **2002**, *99* (17), 10982–10987.

(38) Brédas, J. L.; Beljonne, D.; Coropceanu, V.; Cornil, J. Charge-Transfer and Energy-Transfer Processes in π-Conjugated Oligomers and Polymers: A Molecular Picture. *Chem. Rev.* **2004**, *104* (11), 4971–5003.

(39) Hernández-Martínez, P. L.; Govorov, A. O.; Demir, H. V. Förster-Type Nonradiative Energy Transfer for Assemblies of Arrayed Nanostructures: Confinement Dimension vs Stacking Dimension. *J. Phys. Chem. C* **2014**, *118* (9), 4951–4958.

(40) Alexander Govorov; Pedro Ludwig Hernández Martínez; Hilmi Volkan Demir. *Understanding and Modeling Förster-Type Resonance Energy Transfer (FRET)*; Springer, 2016.

(41) Schrier, J.; Wang, L. Shape Dependence of Resonant Energy Transfer between Semiconductor Nanocrystals. *J. Phys. Chem. C* **2008**, *112* (30), 11158–11161.

(42) Lunz, M.; Bradley, A. L.; Gerard, V. A.; Byrne, S. J.; Gun'Ko, Y. K.; Lesnyak, V.; Gaponik, N. Concentration Dependence of Förster Resonant Energy Transfer between Donor and Acceptor Nanocrystal Quantum Dot Layers: Effect of Donor-Donor Interactions. *Phys. Rev. B* **2011**, *83* (11), 1–10.

(43) Owens, T. G.; Albrecht, A. C. Femtosecond Energy-Transfer Processes in the B800-850. **1991**, *1058*, 280–288.

(44) Freiberg, A.; Godik, V. I.; Pullerits, T.; Timpman, K. Picosecond Dynamics of Directed Excitation Transfer in Spectrally Heterogeneous Light-Harvesting Antenna of Purple Bacteria. *Biochim. Biophys. Acta, Bioenerg.* **1989**, *973* (1), 93–104.

(45) Dostál, J.; Mančal, T.; Augulis, R. N.; Vácha, F.; Pšenčík, J.; Zigmantas, D. Two-Dimensional Electronic Spectroscopy Reveals Ultrafast Energy Diffusion in Chlorosomes. *J. Am. Chem. Soc.* **2012**, *134* (28), 11611–11617.

(46) Laquai, F.; Park, Y. S.; Kim, J. J.; Basché, T. Excitation Energy Transfer in Organic Materials: From Fundamentals to Optoelectronic Devices. *Macromol. Rapid Commun.* **2009**, *30* (14), 1203–1231.

(47) Squire, A.; Verveer, P. J.; Rocks, O.; Bastiaens, P. I. H. Red-Edge Anisotropy Microscopy Enables Dynamic Imaging of Homo-FRET between Green Fluorescent Proteins in Cells. *J. Struct. Biol.* **2004**, *147* (1), 62–69.

(48) Jimenez, R.; Dikshit, S. N.; Bradforth, S. E.; Fleming, G. R. Electronic Excitation Transfer in the LH2 Complex of Rhodobacter Sphaeroides. *J. Phys. Chem.* **1996**, *100* (16), 6825–6834.

(49) Yu, M. N.; Soleimaninejad, H.; Lin, J. Y.; Zuo, Z. Y.; Liu, B.; Bo, Y. F.; Bai, L. B.; Han, Y. M.; Smith, T. A.; Xu, M.; Wu, X. P.; Dunstan, D. E.; Xia, R. D.; Xie, L. H.; Bradley, D. D. C.; Huang, W. Photophysical and Fluorescence Anisotropic Behavior of Polyfluorene β-Conformation Films. *J. Phys. Chem. Lett.* **2018**, *9* (2), 364–372.

(50) Hess, S.; Feldchtein, F.; Babin, A.; Nurgaleev, I.; Pullerits, T.; Sergeev, A.; Sundström, V. Femtosecond Energy Transfer within the LH2 Peripheral Antenna of the Photosynthetic Purple Bacteria Rhodobacter Sphaeroides and Rhodopseudomonas Palustris LL. *Chem. Phys. Lett.* **1993**, *216* (3–6), 247–257.

(51) Grage, M. M. L.; Pullerits, T.; Ruseckas, A.; Theander, M.; Inganäs, O.; Sundström, V. Conformational Disorder of a Substituted Polythiophene in Solution Revealed by Excitation Transfer. *Chem. Phys. Lett.* **2001**, *339* (1–2), 96–102.

(52) Pullerits, T.; Chachisvilis, M.; Sundström, V. Exciton Delocalization Length in the B850 Antenna of Rhodobacter Sphaeroides. *J. Phys. Chem.* **1996**, *100* (25), 10787–10792.

(53) Camacho, R.; Meyer, M.; Vandewal, K.; Tang, Z.; Inganäs, O.; Scheblykin, I. G. Polarization Imaging of Emissive Charge Transfer States in Polymer/Fullerene Blends. *Chem. Mater.* **2014**, *26* (23), 6695–6704.

(54) Camacho, R.; Täuber, D.; Scheblykin, I. G. Fluorescence Anisotropy Reloaded—Emerging Polarization Microscopy Methods for Assessing Chromophores' Organization and Excitation Energy Transfer in Single Molecules, Particles, Films, and Beyond. *Adv. Mater.* **2019**, *1805671*, 1805671.
(55) Camacho, R.; Thomsson, D.; Sforazzini, G.; Anderson, H. L.; Scheblykin, I. G. Inhomogeneous Quenching as a Limit of the Correlation between Fluorescence Polarization and Conformation of Single Molecules. *J. Phys. Chem. Lett.* **2013**, *4* (6), 1053–1058.
(56) Hu, D.; Yu, J.; Wong, K.; Bagchl, B.; Rossky, P. J.; Barbara, P. F. Collapse of Stiff Conjugated Polymers with Chemical Defects into Ordered, Cylindrical Conformations. *Nature* **2000**, *405* (6790), 1030–1033.
(57) Hofkens, J.; Maus, M.; Gensch, T.; Vosch, T.; Cotlet, M.; Köhn, F.; Herrmann, A.; Müllen, K.; De Schryver, F. Probing Photophysical Processes in Individual Multichromophoric Dendrimers by Single-Molecule Spectroscopy. *J. Am. Chem. Soc.* **2000**, *122* (38), 9278–9288.
(58) Bergmann, E. Communications to the Editor. *J. Am. Chem. Soc.* **1932**, *54* (9), 3773–3782.
(59) Camacho, R.; Thomsson, D.; Yadav, D.; Scheblykin, I. G. Quantitative Characterization of Light-Harvesting Efficiency in Single Molecules and Nanoparticles by 2D Polarization Microscopy: Experimental and Theoretical Challenges. *Chem. Phys.* **2012**, *406*, 30–40.
(60) Sirringhaus, H. 25th Anniversary Article: Organic Field-Effect Transistors: The Path beyond Amorphous Silicon. *Adv. Mater.* **2014**, *26* (9), 1319–1335.
(61) Lee, S. Y.; Yasuda, T.; Komiyama, H.; Lee, J.; Adachi, C. Thermally Activated Delayed Fluorescence Polymers for Efficient Solution-Processed Organic Light-Emitting Diodes. *Adv. Mater.* **2016**, *28* (21), 4019–4024.
(62) Hou, J.; Inganas, O.; Friend, R. H.; Gao, F. Organic Solar Cells Based on Non-Fullerene Acceptors. *Nat. Mater.* **2018**, *17*, 119–128.
(63) Rivnay, J.; Inal, S.; Salleo, A.; Owens, R. M.; Berggren, M.; Malliaras, G. G. Organic Electrochemical Transistors. *Nat. Rev. Mater.* **2018**, *3*, 17086.
(64) Zeglio, E.; Inganäs, O. Active Materials for Organic Electrochemical Transistors. *Adv. Mater.* **2018**, *30* (44), 1800941.
(65) Inal, S.; Rivnay, J.; Suiu, A. O.; Malliaras, G. G.; McCulloch, I. Conjugated Polymers in Bioelectronics. *Acc. Chem. Res.* **2018**, *51* (6), 1368–1376.
(66) Adachi, T.; Brazard, J.; Chokshi, P.; Bolinger, J. C.; Ganesan, V.; Barbara, P. F. Highly Ordered Single Conjugated Polymer Chain Rod Morphologies. *J. Phys. Chem. C* **2010**, *114* (48), 20896–20902.
(67) Lin, H.; Tabaei, S. R. S. R. S. R.; Thomsson, D.; Mirzov, O.; Larsson, P. O. P. O. P.-O.; Scheblykin, I. G. I. G. Fluorescence Blinking, Exciton Dynamics, and Energy Transfer Domains in Single Conjugated Polymer Chains. *J. Am. Chem. Soc.* **2008**, *130* (22), 7042–7051.
(68) Täuber, D.; Cai, W.; Inganäs, O.; Scheblykin, I. G. Macroscopic Domains

within an Oriented TQ1 Film Visualized Using 2D Polarization Imaging. *ACS Omega* **2017**, *2* (1), 32–40.
(69) Vohra, V.; Arrighetti, G.; Barba, L.; Higashimine, K.; Porzio, W.; Murata, H. Enhanced Vertical Concentration Gradient in Rubbed P3HT:PCBM Graded Bilayer Solar Cells. *J. Phys. Chem. Lett.* **2012**, *3* (13), 1820–1823.
(70) Anzai, T.; Porzio, W.; Vohra, V. Polarized Emission from Conjugated Polymer Chains Aligned by Epitaxial Growth during Off-Center Spin-Coating. *J. Chem.* **2017**, *2017*, 1–10.
(71) Baliyan, V. K.; Kumar, V.; Kim, J.; Kang, S.-W. Polarized Photoluminescence of the Polymer Networks Obtained by in Situ Photopolymerization of Fluorescent Monomer in a Nematic Liquid Crystal. *Opt. Mater. Express* **2016**, *6* (9), 2956.
(72) Eun Ji Chung; Leon Lorraine; Rinaldi Carlos. *Nanoparticles for Biomedical Applications: Fundamental Concepts, Biological Interactions and Clinical Applications*; Elsevier, 2019.
(73) Zhou, Q.; Bai, Z.; Lu, W. G.; Wang, Y.; Zou, B.; Zhong, H. In Situ Fabrication of Halide Perovskite Nanocrystal-Embedded Polymer Composite Films with Enhanced Photoluminescence for Display Backlights. *Adv. Mater.* **2016**, *28* (41), 9163–9168.
(74) Feng, J.; Yan, X.; Liu, Y.; Gao, H.; Wu, Y.; Su, B.; Jiang, L. Crystallographically Aligned Perovskite Structures for High-Performance Polarization-Sensitive Photodetectors. *Adv. Mater.* **2017**, *29* (16).
(75) He, J.; Towers, A.; Wang, Y.; Yuan, P.; Jiang, Z.; Chen, J.; Gesquiere, A. J.; Wu, S. T.; Dong, Y. In Situ Synthesis and Macroscale Alignment of $CsPbBr_3$ Perovskite Nanorods in a Polymer Matrix. *Nanoscale* **2018**, *10* (33), 15436–15441.
(76) Shi, Z. F.; Li, Y.; Li, S.; Ji, H. F.; Lei, L. Z.; Wu, D.; Xu, T. T.; Xu, J. M.; Tian, Y. T.; Li, X. J. Polarized Emission Effect Realized in $CH_3NH_3PbI_3$ Perovskite Nanocrystals. *J. Mater. Chem. C* **2017**, *5* (34), 8699–8706.
(77) Folie, B. D.; Tan, J. A.; Huang, J.; Sercel, P. C.; Delor, M.; Lai, M.; Lyons, J. L.; Bernstein, N.; Efros, A. L.; Yang, P.; Ginsberg, N. S. Effect of Anisotropic Con Fi Nement on Electronic Structure and Dynamics of Band Edge Excitons in Inorganic Perovskite Nanowires. *J. Phys. Chem. A* **2020**, *124* (9), 1867–1876.
(78) Liu, J.; Hu, F.; Zhou, Y.; Zhang, C.; Wang, X.; Xiao, M. Polarized Emission from Single Perovskite $FAPbBr_3$ Nanocrystals. *J. Lumin.* **2020**, *221* (January), 117032.
(79) Kovalev, D.; Chorin, M. Ben; Diener, J.; Koch, F.; Efros, A. L.; Rosen, M.; Gippius, N. A.; Tikhodeev, S. G. Porous Si Anisotropy from Photoluminescence Polarization. *Appl. Phys. Lett.* **1995**, *67* (May 1995), 1585.
(80) Cunningham, P. D.; Boercker, J. E.; Placencia, D.; Tischler, J. G. Anisotropic Absorption in PbSe Nanorods. *ACS Nano* **2014**, *8* (1), 581–590.

(81) McIntyre, C. R.; Sham, L. J. Theory of Luminescence Polarization Anisotropy in Quantum Wires. *Phys. Rev. B* **1992**, *45* (16), 9443–9446.
(82) Chang, S.; Bai, Z.; Zhong, H. In Situ Fabricated Perovskite Nanocrystals: A Revolution in Optical Materials. *Adv. Opt. Mater.* **2018**, *6* (18).
(83) Meng, L.; Yang, C.; Meng, J.; Wang, Y.; Ge, Y.; Shao, Z.; Zhang, G.; Rogach, A. L.; Zhong, H. In-Situ Fabricated Anisotropic Halide Perovskite Nanocrystals in Polyvinylalcohol Nanofibers: Shape Tuning and Polarized Emission. *Nano Res.* **2019**, *12* (6), 1411–1416.
(84) Zhou, N.; Bekenstein, Y.; Eisler, C. N.; Zhang, D.; Schwartzberg, A. M.; Yang, P.; Paul Alivisatos, A.; Lewis, J. A. Perovskite Nanowire–Block Copolymer Composites with Digitally Programmable Polarization Anisotropy. *Sci. Adv.* **2019**, *5* (5), 1–10.
(85) Lin, C. H.; Kang, C. Y.; Wu, T. Z.; Tsai, C. L.; Sher, C. W.; Guan, X.; Lee, P. T.; Wu, T.; Ho, C. H.; Kuo, H. C.; He, J. H. Giant Optical Anisotropy of Perovskite Nanowire Array Films. *Adv. Funct. Mater.* **2020**, *30* (14), 1–7.
(86) Gao, Y.; Zhao, L.; Shang, Q.; Zhong, Y.; Liu, Z.; Chen, J.; Zhang, Z.; Shi, J.; Du, W.; Zhang, Y.; Chen, S.; Gao, P.; Liu, X.; Wang, X.; Zhang, Q. Ultrathin CsPbX3 Nanowire Arrays with Strong Emission Anisotropy. *Adv. Mater.* **2018**, *30* (31), 1–9.
(87) Ang, D. I. W.; Hi, W. E. N. O. S.; Ing, H. A. O. J.; In, C. H. Y.; Hu, Y. I. Z.; Ing, J. S. U.; A, G. U. O. I. N. M.; Eng, R. U. P.; Ang, X. I. W. Photon-Induced Carrier Recombination in the Nonlayered-Structured Hybrid Organic- Inorganic Perovskite Nano-Sheets. **2018**, *26* (21), 27504–27514.
(88) Motti, S. G.; Meggiolaro, D.; Martani, S.; Sorrentino, R.; Barker, A. J.; De Angelis, F.; Petrozza, A. Defect Activity in Lead Halide Perovskites. *Adv. Mater.* **2019**, *31* (47), 1–11.
(89) Droseros, N.; Longo, G.; Brauer, J. C.; Sessolo, M.; Bolink, H. J.; Banerji, N. Origin of the Enhanced Photoluminescence Quantum Yield in $MAPbBr_3$ Perovskite with Reduced Crystal Size. *ACS Energy Lett.* **2018**, *3* (6), 1458–1466.
(90) Parkinson, P.; Kondratuk, D. V.; Menelaou, C.; Gong, J. Q.; Anderson, H. L.; Herz, L. M. Chromophores in Molecular Nanorings: When Is a Ring a Ring? *J. Phys. Chem. Lett.* **2014**, *5* (24), 4356–4361.
(91) Yong, C. K.; Parkinson, P.; Kondratuk, D. V.; Chen, W. H.; Stannard, A.; Summerfield, A.; Sprafke, J. K.; O'Sullivan, M. C.; Beton, P. H.; Anderson, H. L.; Herz, L. M. Ultrafast Delocalization of Excitation in Synthetic Light-Harvesting Nanorings. *Chem. Sci.* **2015**, *6* (1), 181–189.
(92) Thiessen, A.; Würsch, D.; Jester, S. S.; Aggarwal, A. V.; Idelson, A.; Bange, S.; Vogelsang, J.; Höger, S.; Lupton, J. M. Exciton Localization in Extended π-Electron Systems: Comparison of Linear and Cyclic Structures. *J. Phys. Chem. B* **2015**, *119* (30), 9949–9958.
(93) Camacho, R.; Tubasum, S.; Southall, J.; Cogdell, R. J.; Sforazzini, G.; Anderson, H. L.; Pullerits, T.; Scheblykin, I. G. Fluorescence Polarization

Measures Energy Funneling in Single Light-Harvesting Antennas—LH2 vs Conjugated Polymers. *Sci. Rep.* **2015**, *5* (May), 15080.

(94) Scheblykin, I. G.; Yadav, D.; Pullerits, T. T.; Cogdell, R. J.; Camacho, R.; Meyer, M.; Tubasum, S.; Camacho, R.; Meyer, M.; Yadav, D.; Cogdell, R. J.; Pullerits, T. T.; Ivan G. Scheblykin. Evidence of Excited State Localization and Static Disorder in LH2 Investigated by 2D-Polarization Single-Molecule Imaging at Room Temperature. *Phys. Chem. Chem. Phys.* **2013**, *15* (45), 19862–19869.

(95) Lin, H.; Camacho, R.; Tian, Y.; Kaiser, T. E.; Würthner, F.; Scheblykin, I. G. Collective Fluorescence Blinking in Linear J-Aggregates Assisted by Long-Distance Exciton Migration. *Nano Lett.* **2010**, *10* (2), 620–626.

(96) Shi, J.; Xu, X.; Xia, Y.; Chen, R.; Hawash, Z.; Deribew, D.; Moons, E.; Inganäs, O.; Scheblykin, I. G. Photo-Oxidation Reveals H-Aggregates Hidden in Spin-Cast-Conjugated Polymer Films as Observed by Two-Dimensional Polarization Imaging. *Chem. Mater.* **2019**.

(97) Camacho, R.; Täuber, D.; Hansen, C.; Shi, J.; Bousset, L.; Melki, R.; Li, J.-Y.; Scheblykin, I. G.; Ivan G. Scheblykin. 2D Polarization Imaging as a Low-Cost Fluorescence Method to Detect α-Synuclein Aggregation Ex Vivo in Models of Parkinson's Disease. *Commun. Biol.* **2018**, *1* (1), 157.

(98) Mirzov, O.; Bloem, R.; Hania, P. R.; Thomsson, D.; Lin, H.; Scheblykin, I. G. Polarization Portraits of Single Multichromophoric Systems: Visualizing Conformation and Energy Transfer. *Small* **2009**, *5* (16), 1877–1888.

(99) Ohzono, T.; Yatabe, T.; Wang, C.; Fukazawa, A.; Yamaguchi, S. Negative Fluorescence Anisotropy of Phosphole Oxide-Based Dyes in Nematic Liquid Crystals. *Commun. Chem.* **2018**, *1* (1), 1–9.

(100) Shi, X.; Basran, J.; Seward, H. E.; Childs, W.; Bagshaw, C. R.; Boxer, S. G. Anomalous Negative Fluorescence Anisotropy in Yellow Fluorescent Protein (YFP 10C): Quantitative Analysis of FRET in YFP Dimers. *Biochemistry* **2007**, *46* (50), 14403–14417.

(101) Neuhaus, P.; Cnossen, A.; Gong, J. Q.; Herz, L. M.; Anderson, H. L. A Molecular Nanotube with Three-Dimensional π-Conjugation. *Angew. Chem.* **2015**, *127* (25), 7452–7456.

(102) Scheblykin, I. G.; Drobizhev, M. A.; Varnavsky, O. P.; Van Der Auweraer, M.; Vitukhnovsky, A. G. Reorientation of Transition Dipoles during Exciton Relaxation in J-Aggregates Probed by Fluorescence Anisotropy. *Chem. Phys. Lett.* **1996**, *261* (1–2), 181–190.